International Journal of Heat and Mass Transfer 194 (2022) 123070

Contents lists available at ScienceDirect

International Journal of Heat and Mass Transfer

journal homepage: www.elsevier.com/locate/hmt

Thermal conductivity analysis of porous NiAl materials manufactured by spark plasma sintering: Experimental studies and modelling

Szymon Nosewicz[a,*], Grzegorz Jurczak[a], Tomasz Wejrzanowski[b], Samih Haj Ibrahim[b], Agnieszka Grabias[c], Witold Węglewski[a], Kamil Kaszyca[c], Jerzy Rojek[a], Marcin Chmielewski[c]

[a] Institute of Fundamental Technological Research, Polish Academy of Sciences, 5B Pawinskiego, 02-106 Warsaw, Poland
[b] Warsaw University of Technology, 141 Woloska Str, 02-507 Warsaw, Poland
[c] Lukasiewicz Research Network, Institute of Microelectronics and Photonics, 32/46 Al. Lotników Str, Warsaw, 02-668, Poland

ARTICLE INFO

Article history:
Received 5 April 2022
Revised 17 May 2022
Accepted 21 May 2022

Keywords:
Thermal conductivity
Porous materials
Spark plasma sintering
Micro-computed tomography
Nickel aluminide
Finite element modelling
Tortuosity

ABSTRACT

This work presents a comprehensive analysis of heat transfer and thermal conductivity of porous materials manufactured by spark plasma sintering. Intermetallic nickel aluminide (NiAl) has been selected as the representative material. Due to the complexity of the studied material, the following investigation consists of experimental, theoretical and numerical sections. The samples were manufactured in different combinations of process parameters, namely sintering temperature, time and external pressure, and next tested using the laser flash method to determine the effective thermal conductivity. Microstructural characterisation was extensively examined by use of scanning electron microscopy and micro-computed tomography (micro-CT) with a special focus on the structure of cohesive bonds (necks) formed during the sintering process. The experimental results of thermal conductivity were compared with theoretical and numerical ones. Here, a finite element framework based on micro-CT imaging was employed to analyse the macroscopic (effective thermal conductivity, geometrical and thermal tortuosity) and microscopic parameters (magnitude and deviation angle of heat fluxes, local tortuosity). The comparison of different approaches toward effective thermal conductivity evaluation revealed the necessity of consideration of additional thermal resistance related to sintered necks. As micro-CT analysis cannot determine the particle contact boundaries, a special algorithm was implemented to identify the corresponding spots in the volume of finite element samples; these are treated as the resistance phase, marked by lower thermal conductivity. Multiple simulations with varying content of the resistance phase and different values of thermal conductivity of the resistance phase have been performed, to achieve consistency with experimental data. Finally, the Landauer relation has been modified to take into account the thermal resistance of necks and their thermal conductivity, depending on sample densification. Modified theoretical and finite element models have provided updated results covering a wide range of effective thermal conductivities; thus, it was possible to reconstruct experimental results with satisfactory accuracy.

1. Introduction

Thermal conductivity is one of the most relevant functional properties of porous materials. Depending on their specific application, they can provide low thermal conductivity when operated as thermal barrier coatings [1], thermal insulators [2], or contribute increased conductivity for application in electronic devices, nuclear fuels, or thermoelectric materials [3].

Porous materials are composed of rambling structures at a microscopic scale. Thus, the flow path during heat transfer is tortuous and meandering [4]. Contrary to crystalline materials, pores restrict heat transfer very effectively as the thermal conductivity of air (or gas) is very low. Even the presence of the additional modes of the heat transfer, i.e., radiation (negligible at low temperatures) and convection (negligible for small pores) is insufficient to compensate for the effect of low heat transport through the pores, as these effects can be largely ignored [5,6]. They are several microstructural parameters specified by porous media in the context of heat transfer, such as porosity degree, pore and particle size distribution, specific surface area, and tortuosity. As one example, depend-

* Corresponding author.
E-mail address: snosew@ippt.pan.pl (S. Nosewicz).

https://doi.org/10.1016/j.ijheatmasstransfer.2022.123070

ing on medium characteristics, the pores can be elongated and interwoven to demonstrate an elevated porosity and anisotropy, such as in fibrous media [7], whereas, on the contrary, they exhibit low porosity with a tight network of twisted channels [8].

When we consider heat conduction phenomena, all the investigated microstructural features can be summarised by effective thermal conductivity, λ_{eff}, which represents the macroscopic response of the whole range of porous materials. Numerous analytical models devoted to calculating λ_{eff} can be found in the literature, e.g., series and parallel models approach assuming sequential layers normal or parallel to the heat flux, and provide lower and upper bounds for λ_{eff} [9]. Maxwell–Eucken, effective medium theory, Levy and Kopelman models for λ_{eff} are also known [9]. Unfortunately, the ability to predict the thermal conductivity of porous materials is limited and marked by a significant level of uncertainty, due to the oversimplification of the physical microstructure of the material. Such models usually assume simple 2D arrays or small representative 3D arrays for a whole porous sample, and estimate λ_{eff} as a function of microstructural parameters.

A special type of porous materials is those manufactured by sintering techniques [10]. Recently, a large effort has been made in modelling of heat transfer through packed [11,12] and sintered [13–18] collective particles representing the powder. Most of the mentioned models regarding sintered materials are semi-empirical approaches developed to predict λ_{eff} [13-15,17]. They can be treated as a combination and/or extensions of the sintering neck growing theory initially delivered by Ashby [19] and/or the particle contact model for thermal conduction between spheres [20]. Such models are devoted to the theoretical understanding of microstructure (neck growth, densification) during sintering and its impact on thermal conductivity in terms of several sintering process parameters, such as sintering temperature, time, and compressive pressure. Aside from the many advantages of proposed models, such as a distinctive investigation of neck growth based on diffusion mass transport mechanism and experimental validation of obtained results, they have also demonstrated considerable limitations regarding the simplistic representation of microstructure evolution (i.e., the arrangement of perfectly spherical particles with the same size) and unrealistic assumptions of heat conduction, such as heat only being transferred in the vertical straight direction. Thus, planes perpendicular to the direction of heat flow are isothermal [13].

The complexity of porous, sintered or any other heterogeneous materials sets the bar high for any modelling approach applied to calculate their effective physical properties. Multiple variables related to composition changes, the presence of inclusions/pores of different types and shapes, thermal anisotropy, and orientation-sensitive thermal properties of structural components can be successfully identified in the sample model using numerical simulations. Various numerical methods have been used to examine effective thermal properties of the sample, ranging from finite element method (FEM) [21–24] to particle modelling approaches [25–28].

Since the precise arrangement of porous materials appears to be the key factor for λ_{eff} evaluation, a highly efficient approach is based on image analysis of the microstructure photography, which allows for deeper and more precise insight into the real microstructure of the material via full 3D particle and void distributions [4]. Accurate reconstruction of the inhomogeneous 3D microstructure of the material and further simulation of thermal or mechanical properties is possible via the use of the micro-computed tomography (micro-CT) technique, which is based on X-ray tomographic imaging [24,29,30]. X-rays allow for precise slice-by-slice mapping of the sample and its spatial resolution reaches 100 nm, while scanned objects can be as large as 200 mm in diameter. The combination of FEM simulation and micro-CT imaging

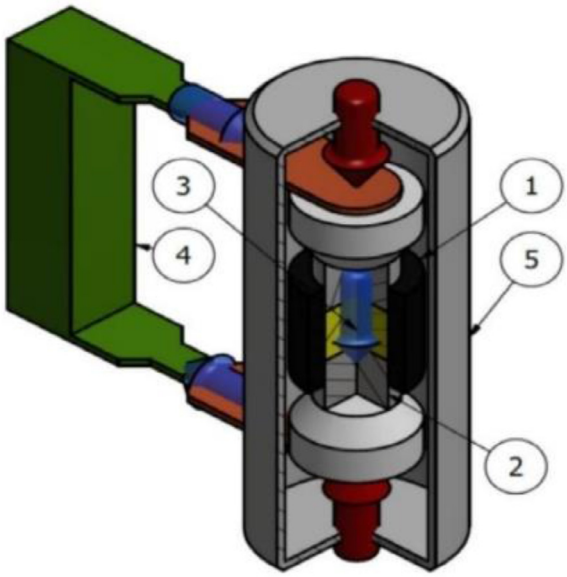

Fig. 1. SPS apparatus: 1 -graphite die, 2 – graphite punches, 3 – sample (NiAl powder), 4 – electrical supply, 5 – vacuum chamber

appears to have great potential and can be applied in different areas, such as powder metallurgy.

Regarding the advantages and limitations of models found in the literature, the proposed work employs the numerical model of heat conduction based on a finite element framework, utilising the real representation of sample microstructures obtained by micro tomography. Numerical results of λ_{eff} are complemented by analytical results from three straightforward theoretical relations, based on the theory of a two-phase mixture. Finally, the modelling predictions have been verified by experimental results of λ_{eff} of previously-sintered samples.

The proposed paper attempts to link the sintering process parameters, the microstructure and the thermal properties, evaluated in both macro- and microscopic scales, for nickel aluminide (NiAl) samples. Here, we use spark plasma sintering (SPS) as the manufacturing method, which recently has become a commonly-used technology for powder consolidation [31]. The description of the spark plasma sintering approach is presented in next section.

2. Methods and methodology

2.1. Experimental techniques – manufacturing and characterisation

In the presented work, intermetallic NiAl was selected as the representative material for thermal conductivity analysis. NiAl powder (Goodfellow, purity 99.9%, gas atomised) was sintered via SPS method (Fig. 1). In this technique, direct electric current flow is applied to heat the powders and die, while simultaneously accelerating the sample densification by applying a uniaxial mechanical load. The powder particle surfaces are more easily purified and activated than in conventional electrical sintering processes, and material transfers at both the micro and macro levels are promoted; thus, a high-quality sintered compact is obtained at a lower temperature and in a shorter time than by conventional processes [32]. Moreover, a decisive advantage of the SPS resulting from the short process time is related to the possibility to sinter materials without significant grain growth, which has fundamental importance for the manufacturing of nanomaterials [33]. Powder morphology and manufacturing conditions such as sintering temperature, time, atmosphere, assisted pressure, and heating and cooling rate should

be treated as the most important factors influencing the densification rate of sintered materials.

The aim of the technological task was to obtain a material with a diversified rate of densification. To achieve this goal, the sintering conditions were selected based on preliminary tests. The samples were heated at a rate of 100 K/min to target sintering temperature, T_s (within the range of 1100–1300°C), and maintained under external pressure p (5 or 30 MPa) for 10 min of sintering time, t_s. The final size of the disc-shaped samples was 25 mm in diameter and 10 mm in height. Discs were cut to provide samples for further research.

Density and thermal conductivity measurements were conducted for sintered NiAl at different degrees of material densification. Material density was measured using the hydrostatic method, based on Archimedes' principle. The densification degree was approximated by the relative density, d_{rel}, defined as the ratio of the measured bulk density and the theoretical density of NiAl material ($d_{NiAl} = 5.91$ g/cm^3). The thermal conductivity of sinters, λ_{exp}, was estimated based on thermal diffusivity measurements using laser flash method (LFA 457, Netzsch) according to the procedure previously described [34].

Sintered porous NiAl samples were investigated in the context of microstructural evolution using scanning electron microscopy (Auriga, Zeiss) and X-ray CT. The latter experimental tool was also used to obtain the geometrical representation of porous structures essential for the numerical work.

X-ray CT studies were carried out using an EasyTom system (RX Solutions, Chavanod, France), with a nano-focus open transmission X-ray source with a tungsten target and a diamond window and a PaxScan 2520DX Varian flat panel detector. X-ray CT was performed for samples in the form of cubes with approximate dimensions of $2 \times 2 \times 2$ mm^3. The isotropic voxel size, resulting from the geometrical configuration, was kept constant at 1.83 µm for all samples. The total number of projections taken was 2880. The images were acquired at a tube voltage of 160 kV and target current of 35 µA in a continuous cone beam single circle acquisition mode with an additional 32 reference images. The tomographic reconstruction and further data analysis were performed using the manufacturer's X-Act and commercial VGSTUDIO MAX software.

2.2. Modelling approach of heat conduction of porous materials

2.2.1. Theoretical background of heat conduction

Heat transfer describes the flow of thermal energy and temperature distribution, as well as changes caused by a temperature gradient. The transport of thermal energy is classified into three mechanisms: conduction, convection, and radiation. These mechanisms may occur simultaneously despite their distinct characteristics and intensity. Radiation and convection occur through the pores in porous media but their intensity is much smaller, mainly due to the limited potential for thermal transport. In the case of solid materials, the most important mode of heat transfer is thermal conduction. There are two well-known types of heat conduction: electrons movement and lattice vibration (phonons) [35]. In metallic materials, the heat transfer occurs mainly in an electronic way, while the lattice component is usually minor. On the contrary lattice vibrations are the dominant carriers of heat for semiconductors and insulating materials [36]. Intermetallics, such NiAl investigated in this work, may indicate one of the mentioned above behaviour or their combination [37]. The proportion between phonons or electronic mechanisms depends on many factors e.g. temperature, chemical and phase composition, electronic and crystal structure, grain size, impurity levels, porosity and phase distributions [38]. In particular, the study of the dominant carrier of thermal conduction of stoichiometric NiAl compounds through electrical conductivity measurements and the Wiedemann Franz law brought the conclusion of the decisive predominance of electron type rather than a phonon one [37]."

Mathematical description of the heat transfer in conduction mode assumes heat flux to be proportional to the negative temperature gradient. Such a classical approach is described by Fourier's law:

$$\vec{q} = -\lambda \nabla T \tag{1}$$

where q denotes the vector of heat flux, λ is the constant of proportionality, known as thermal conductivity, and ∇T is the temperature gradient. If we consider a one-dimensional problem, where the direction of the heat flow is clear, then we may simplify the formula to the scalar form:

$$q = -\lambda \frac{\Delta T}{L} \tag{2}$$

where ΔT is temperature difference and L is the thickness of the body.

In the case of polycrystalline materials, heat transfer depends on the spatial distribution of the components and, of course, on their thermal conductivity. To describe averaged thermal properties of heterogeneous materials, the so-called "effective thermal conductivity" (i.e., λ_{eff}) has been introduced. λ_{eff} of polycrystalline or porous materials can be defined by modifying Eq. (2), where local thermal conductivity is replaced by the effective global coefficient λ_{eff} describing spatially averaged heat flow. The effective coefficient takes into account disturbance of the heat flow, related not only to different thermal properties of the sample components but also the presence of inclusions, grain boundaries (GBs), pores, and other sources [39]:

$$\lambda_{eff} = -\frac{QL}{\Delta TA} \tag{3}$$

where Q is total heat ($\Sigma q_i A_i$) transferred and A is overall surface area.

Polycrystalline materials exhibit reduced thermal conductivity compared to their corresponding bulk single crystals due to the effect of GBs [40]. In the context of sintering, such interfaces occur in the form of necks or cohesive bonds. As heat is conducted across an interface between the contacting grains or particles, a temperature drop occurs at the boundary. This effect is known as interfacial thermal resistance (ITR), and is treated as the combination of thermal contact resistance (TCR) and thermal boundary resistance (TBR). TCR originates from undeveloped and imperfect mechanical contact between solids (e.g., grains or particles) due to surface roughness and other effects [41]. Different analytical and experimental studies have been performed to demonstrate the importance of surface roughness in TCR [42–44]. One of the most straightforward approaches assumes that the particles (in the form of discrete elements) are covered by a thin layer with a lowered thermal conductivity [25,26].

TBR, known as the Kapitza resistance, considers GBs as obstacles toward heat conduction by scattering heat carriers [45]. The concept of the Kapitza, introduced by Nan and Birringer [40], and its incorporation within the effective medium allows us to predict the thermal conductivity of polycrystalline solids with isotropic, equally-sized spherical crystallites. The model was later slightly modified by Yang et al. [46]:

$$\lambda_s = \frac{\lambda_c}{1 + \frac{R\lambda_c}{d}} \tag{4}$$

where λ_c is the crystalline (or grain) thermal conductivity, d is the grain size and R is the thermal resistance for a grain boundary of unit area.

Analogically, λ_{eff} and its reduction due to the Kapitza resistance can be estimated by the brick layer model [39]. This model

is based on the assumption that the whole of the GBs can be collected together as one resistance and all the crystallite cells can be grouped as another resistance. This expression states that the effective resistance is a sum of the intrinsic resistance plus the sum of the resistances for each boundary crossed [47].

Both microscopic models – the Yang and brick layer models – demonstrate the influence of interfacial thermal resistance on the decrease in λ_{eff}, which is highly manifested for fine-grained polycrystals [48] as well as for sintered materials [13]. Recently, several numerical and theoretical methods have been developed with an aim to model the ITR [45,47,48]. All these approaches are based on an analytical relation assuming that a temperature jump ($\Delta T'$) exists at the solid-solid contact surface (or GB):

$$R = \Delta T/q \tag{5}$$

where q is the heat flow rate, and ΔT is the temperature difference between two adjacent solid-solid contact surfaces [41].

2.2.2. Analytical models of effective thermal conductivity of porous materials

Generally, theoretical methods of evaluation of the λ_{eff}, in terms of material porosity, consider the mixture of two phases, solid and pores, in a similar way as a metal matrix composite [49] or other multi-phase materials. Such models neglect the radiation phenomenon and simply concern the heat transfer within the solid and gas phases. Selection of an adequate model depends on the porosity range, pore shape and other microstructural features [39]. For materials from with relative densities between 0.65 and 1, several theoretical approaches can be used. The simplest expression based on a volumetric law of mixtures, known as the parallel relation and which designates the upper limit, averages the conductivities as follows [50]:

$$\lambda_{eff} = \lambda_s(1 - \upsilon_p) + \upsilon_p\lambda_p \tag{6}$$

where λ_s is the thermal conductivity of the solid, λ_p is the thermal conductivity of the pores and υ_p is the pore volume fraction.

The Maxwell–Eucken relation, or equivalently Hashin and Shtrikman [51], have been ultimately introduced to predict the magnetic permeability in two-phase composites, limited to materials with a closed porosity fraction lower than 15% and with pores distributed uniformly in the solid medium. In many works, this has been employed effectively to evaluate macroscopic properties from heat conduction analysis [39,52]:

$$\lambda_{eff} = \lambda_s \frac{\lambda_p + 2\lambda_s + 2\upsilon_p(\lambda_p - \lambda_s)}{\lambda_p + 2\lambda_s - \upsilon_p(\lambda_p - \lambda_s)} \tag{7}$$

In the porosity range up to 0.65, the Landauer formula, based on effective medium percolation theory, has become the standard theoretical method of λ_{eff} evaluation [53]. The model describes a straightforward, physically insightful characteristic of ballistic transport predicting heat flow in solid or porous media, such as nanostructures [54,55]. This relationship was derived from analysis of the process of heat conduction through a medium with a random distribution of both phases, and the apparent presence of open porosity connecting the multiple channels:

$$\lambda_{eff} = 0.25\Big[\lambda_p(3\upsilon_p - 1) + \lambda_s(2 - 3\upsilon_p) + \Big\{[\lambda_p(3\upsilon_p - 1) + \lambda_s(2 - 3\upsilon_p)]^2 + 8\lambda_s\lambda_p\Big\}^{0.5}\Big] \tag{8}$$

2.2.3. Finite element framework based on micro-CT

The numerical investigation of thermal conductivity of SPS samples has been performed by finite element analysis based on X-ray computed tomography imaging. The main aim of finite element simulation of heat conduction is to calculate the λ_{eff} of a sintered NiAl sample, together with the characterisation of samples in terms of the microstructural and thermal properties at the microscopic scale. The numerical procedure consists of three main steps: (1) data transfer from micro-CT to the finite element model, (2) solution of the thermal problem, and (3) calculation of the λ_{eff} on the basis of resultant heat fluxes.

The first step consists of the import of a set of micro-CT images (Fig. 2) into the ScanIP/ScanFE package [56] and the selection of a part of the sample volume for mesh generation. In the selected part of the 3D image representation, one has to assign a mask for each phase [57]. For materials with good contrast between phases, this can be easily done by setting threshold levels of grayscale using the "*Threshold*" function in the ScanIP/ScanFE software. By implementing the thresholds, we can obtain the mapped NiAl and pores sections (Fig. 2). Finally, the software provides finite element mesh, consisting of cube elements with edge size 1.83 μm. Each element is identified as either a particle or pore; hence, the spatial distribution of the elements repeats a real structure of the sample.

The size of the examined region of interest (ROI) should be assigned carefully to represent a microstructural cell fulfilling the requirement of statistic homogeneity for the set of micro-scale elements (particles and pores) [58]. Based on the homogeneity study of sintered NiAl presented in section 3.1.2 for FEM calculations, we chose samples consisting of 100 × 100 × 100 DC3D8 thermally conductive elements, with averaged porosity attuned to those measured experimentally.

One of the FEM pre-processing steps is the assumption of the boundary conditions. In this case, boundary conditions are related to the temperature on the bottom and top faces of the sample, assumed to be 0 and 100°C, respectively. Side facets of the sample completely block out the heat flow normal to these surfaces by default, equivalent to its adiabatic behaviour (Fig. 2). In addition, proper thermal conductivity coefficients related to the NiAl solid and pores, λ_s and λ_p, are assumed to be 88.5 and 0.05 W/mK, respectively. Thermal conductivity of NiAl keeps constant value along with different samples since the application of various sintering process parameters does not affect the powder particles themselves and only the contacts (necks) between them [49,59]. A non-zero value of the thermal conductivity through the pores is the way to avoid singularity; therefore, the numerical problem of "*hanging*" grains (no connectivity with other grains) appears in samples.

We consider the steady-state thermal conductivity problem via thermal boundary-value problem formulation and implement its solution by use of finite element method approach within the Abaqus package [60]. Solution of the steady-state problem provides the spatial distribution of the temperature and heat fluxes. To calculate λ_{eff} of the sample, we have to calculate total heat perpendicular to the bottom surface as a sum of the individual nodal fluxes times the specific area of the finite element related to that flux. Later, this sum is divided by the height of the sample and temperature difference, as stated in Eq. (3).

2.2.4. Tortuosity

Tortuosity is one of the most important properties of porous materials [61], and is a considerable research interest in many scientific and engineering fields [62–64]. The tortuous factor, τ, can be defined as a quantitative parameter of the flow decay induced by the sinuous path imposed by the physical barrier, compared to the straightest path in an unrestricted medium, in the direction of the flow [65]. Although there is no rigorous and unique definition for tortuosity as its physical essence is not completely understood [4], tortuosity has been used to describe the transport behaviour of several physical media and materials, such as fluids, molecules/atoms, electrical current and heat transfer, and thereby affects their macroscopic equivalents, such as thermal conductivity.

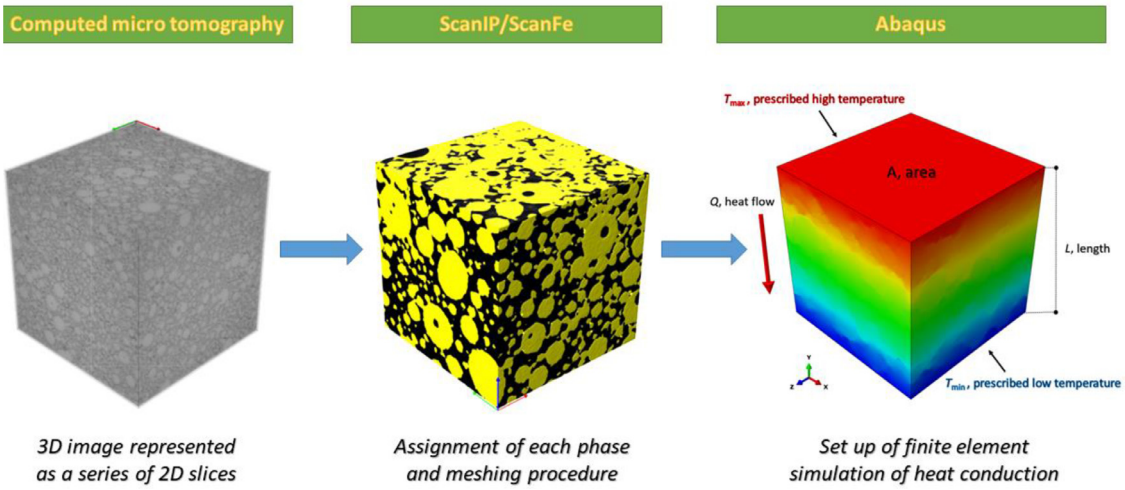

Fig. 2. A schematic overview of finite element framework of heat transfer based on micro-CT.

A comprehensive review of different kinds of tortuosity in porous media is presented elsewhere [4].

In this study, due to the investigated phenomenon, *the geometrical* (based on micro-CT analysis) and *thermal phenomenological tortuosity* (based on FEM results) have been evaluated and analysed in the context of densification of NiAl samples and their thermal properties. To reveal the streamline level deviating from a straight line in sintered samples, geometrical tortuosity is calculated as the ratio of the effective length of flow paths L_g to the straight-line distance L in the macroscopic flow direction:

$$\tau_g = \frac{L_g}{L} \tag{9}$$

The effective length of flow path L_g can be evaluated from the digital 2D or 3D representations of the microstructure (obtained by micro-CT, SEM, FIB and FEM) via several image analysis methods, including the direct shortest-path search method (DSPSM) [65], the skeleton shortest path search method (SSPSM) [66], the fast marching method (FMM) [67] and the pore centroid method (PCM) [68]. A combination of DSPSM and PCM approaches has been employed here, based on 3D finite element mesh determined from micro-CT analysis. L_g is treated as the minimum path through finite elements of the solid material from top to bottom (Fig. 3). The algorithm describing flow has been developed based on several key assumptions:

- the 26-neighbour-connectivity criterion during the patch searching algorithm using six faces, 12 edges and eight vertices of finite elements,
- the selection criterion of the shortest path from element to element starting from the contacts by faces, edges and then vertices,
- in the case of multiple elements with equal distance, selection of the element occurs by picking the closest one to the axis of prescribed flow, designated by the top starting element,
- in order to minimise the path in the horizontal direction, the route of flow is restricted to the channel with a size of 20 elements with a central axis of prescribed flow,
- each flow is optimised by a smoothing procedure, lowering the element-element path in cross-section of channels of solid materials elements.

With these assumptions in mind, the effective length of flow path L_g can be defined as the sum of local element-to-element length and is calculated as follows:

$$L_g = \sum_{i=1}^{n-1} \sqrt{(x_{i+1} - x_i)^2 + (y_{i+1} - y_i)^2 + (z_{i+1} - z_i)^2} \tag{10}$$

where i is the number of iterations, n is the total number of iterations (in most cases equal the number of 2D slices in 3D sample), and x_i, y_i, and z_i are the coordinates of the finite element representing the solid material.

Since the path of geometrical tortuosity models may take into account the sintered microstructure with all features (e.g., pores number, shapes), thermal tortuosity considers the details of the heat transport mechanism occurring within the volume of solid material. The idea of thermal tortuosity refers to the sinuous characteristics of heat paths, permitting capture of the heat flow perturbation in porous media [69]. Analytically, thermal tortuosity can be determined by taking into account λ_{eff}, bulk conductivity of a solid medium λ_s and its relative density d_{rel} [4,69,70]:

$$\tau_t = \sqrt{\frac{\lambda_s}{\lambda_{eff}}(1 - d_{rel})} \tag{11}$$

Taking advantage of the thermal and geometrical features, we propose a simple method of thermal tortuosity evaluation. This phenomenological approach is essentially based on the results from the FEM simulation of heat transfer and concerns the vectors of heat fluxes $\vec{q}$, which indicates the preferred direction of flow (Fig. 3). Angles between the heat flux vector of the reference element $\vec{q}_r$ and the vectors from the reference element to first-order neighbours α_i are calculated. The neighbour with the lowest angle is selected as the next reference element and, therefore, creates the path. As in the geometrical tortuosity evaluation, the 26-neighbour-connectivity criterion and smoothing procedure have been adopted in the proposed methodology. The effective length of flow path L_g is calculated via Eq. (10) and thermal phenomenological tortuosity using Eq. (9). The calculated tortuosity τ_t, as well as geometrical tortuosity, is a scalar parameter greater than one and is generally presented as the average value from multiple number runs/flows.

It should be noted that both algorithms, describing geometrical and thermal phenomena, have been implemented in their own C# code. Furthermore, the performance of both methods has been verified by a manual approach, checking over slice-by-slice the correctness of the path for a certain number of flows and obtaining the required convergence. With the algorithms validated, the

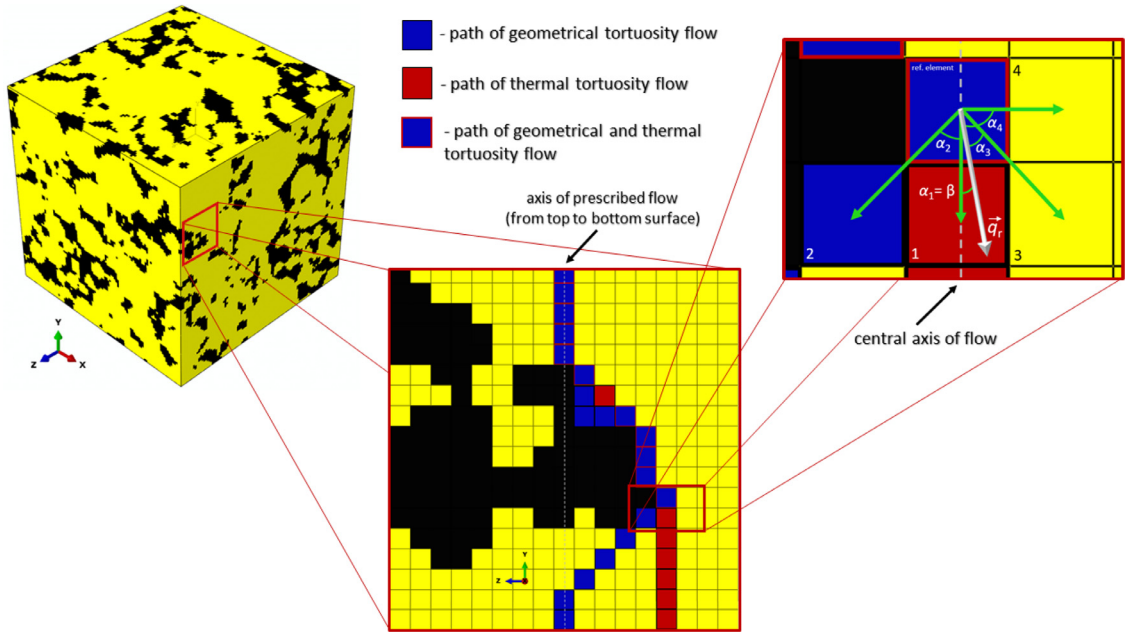

Fig. 3. Schematic diagram of methodology of geometrical and thermal phenomenological models.

geometrical and thermal phenomenological approaches have been used to study six sintered samples.

3. Results and discussion

3.1. Characterisation of porous samples

3.1.1. Microstructural study

Sintering is defined as a thermally-activated process that occurs at high temperatures and leads to loose particles' transformation into a solid material. The progress of the sintering process is measured via two phenomena: an increase in the cross-section of an inter-grain neck, as well as a decrease in the distance between the centres of two neighbouring grains. There is a great scientific interest focused on the issues related to the mechanisms of neck formation and neck growth during the sintering process, especially for conducting powders [18, 71-73]. The phenomena accompanying the material densification process in the case of sintering via SPS are unclear and still require systematic investigation. Based on the microstructural analyses, the mechanisms of material densification can be explained and described.

The starting point of the sintering process is usually assumed to be the point when particles of the powder are touching. In the SPS method, as the electric current starts to flow, the elimination of oxide layers and absorbed gases on the surface of powder particles is promoted. While the particle surfaces are cleaned and activated, an increase in material density and pore elimination is observed due to the diffusion processes along with temperature rise. To visualise this evolution, the micro-CT data of the real sintered structures was processed to visualise 2D images of three representative cross-sections of the studied cube samples and their 3D reconstructions (Fig. 4). The 2D images of sample 1 (T_s = 1100°C, p = 5 MPa) reveal round-shaped bright metallic particles separated by dark regions, originating from a significant porosity. Some of the particles have a dark spot inside, indicating that the starting powder also contains hollow particles. It is worth mentioning that a quantitative analysis of the CT data of the starting intermetallic powder provided detailed information regarding the distribution of particle sizes, in which the majority of the metallic particles had

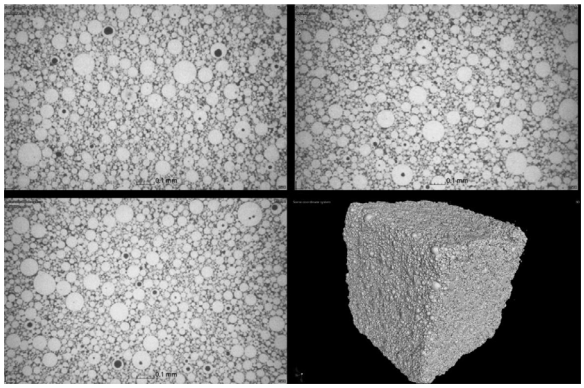

Fig. 4. X-ray computed tomography images of sample 1.

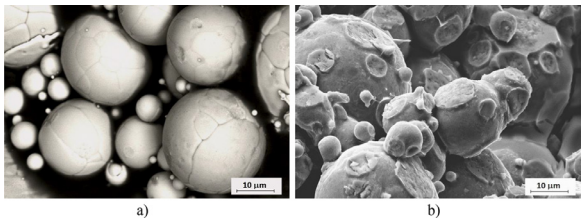

Fig. 5. SEM images of NiAl fractures at initial stage of sintering of: a) sample 1 (T_s=1100°C, p=5 MPa), d_{rel}=70.2% and b) sample 3 (T_s=1300°C, p=5 MPa), d_{rel}=84.4%.

diameters in the range of several microns with an average value d_{avg} = 9.2 µm.

The forming of the first necks between the NiAl particles can be observed in Fig. 5a. There are some visible single traces showing the contact of individual particles with each other. At the beginning of the sintering process, the neck size is small and their physical properties (strength, conductivity) are significantly reduced. When the sintering temperature is increased up to 1300°C (Fig. 5b), a significant increase in densification rate is observed; this is related to an increase in the number of necks and in neck size, confirming the progression of the sintering process.

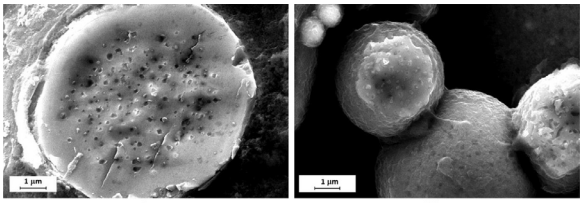

Fig. 6. SEM images of NiAl neck formation during sintering of: a) sample 3 (T_s=1300°C, p=5 MPa), d_{rel}=84.4% and b) sample 4 (T_s=1100°C, p=30 MPa), d_{rel}=89.3%.

The neck size at this stage of sintering was estimated to be within the range of 1 to 10 μm, depending on the size of two adjacent particles. The rate of increase in contact area is most rapid at the initial stage of sintering. A similar observation was made in previous reports [49,59, 72], wherein the neck growth was rapid at the beginning, slowed down later on, and finally approached zero. Such behaviour was explained by the fact that the curvature difference at the contact zone is large at the initial stage of sintering, and with neck growth the curvature is reduced, implying the reduction of driving forces. This finally affects the approach of the centres of adjacent grains, clearly visible in Fig. 5b.

The limited state and quality of necks with a visible number of cracks and discontinuities across the neck (Fig. 6a) seems to strongly influence the mechanical strength and thermal conductivity of sinters. This observation corresponds well to the behaviour of sintered pure copper [71], where neck structures with fine dimples were noticed. Furthermore, it was suggested that fine grains in the neck zones can be formed first through a process of local melting and then rapid solidification, which is precisely the process of neck formation. At this stage of sintering, high local temperature gradients or non-uniform temperature distribution can be observed. Similarly for microwave sintering, surface diffusion seems to be the most important densification mechanism during the early stages of sintering, although a liquid phase is suggested too [72].

In the case of NiAl sintering via SPS method in this work, no evidence of material melting was observed. For sample 4 (manufactured in T_s = 1100°C, p = 30 MPa, d_{rel} = 89.3%), the density of which is relatively close to that of sample 3 (T_s = 1100°C, p = 5 MPa, d_{rel} = 84.4%), the structure of the neck is more compact (Fig. 6b), and only some local pores can be distinguished in the fracture area. Moreover, as sintering progresses the amount of necks formed increases. An increase in contact number directly influences the speed of densification during the SPS process; thus, the time required for obtaining near-fully dense materials is relatively short compared to conventional sintering techniques.

External pressure plays an important role in the densification process, as it directly impacts the sintering mechanisms by intensifying the phenomena that occur during the process, increasing the rate of sintering. Simultaneously, the lower sintering temperature limits the grain growth of the material. The quality of the bonding between adherent grains (sample 4) appears to be stronger and more durable. Additionally, the external pressure facilitates pore elimination processes in the final stages of sintering. The joint interaction of temperature and pressure leads to obtaining a material with a relatively low level of total porosity (sample 6 T_s = 1100°C, p = 30 MPa, d_{rel} = 97.5%). It should be noted that in the case of sample 6 with near-full densification, we refer to well-developed grain boundaries instead of necks, as in the case of materials with a lower degree of densification. The fracture occurs mostly through the grain boundaries or grains themselves, confirming the high-quality connections between the grains (Fig. 7).

In conclusion, the properties of porous materials depend on many factors, the most important being total porosity amount, average pore size, and their shape and distribution in a material's structure [74]. A good correlation between modelling and experimental results of sintered NiAl based materials was presented in our previous work [49], wherein the relationships between microstructure and mechanical properties were examined. An equally important issue is the thermal conductivity of materials containing a significant number of pores [15]. Heat and mass transport plays a very important role in the case of the material densification process via SPS. The electric current flow through a system of loose particles causes a local temperature increase in the contact area. Next, the whole volume is heated due to the Joule effect with a rapid increase in the temperature (up to 2000°C with rates up to 10K/s). Heat flux directly influences the mass transport mechanisms responsible for the sintering phenomenon. The directed current flow can create privileged sintering directions of the powder, which can result in varying material densification rates and varying material properties in different directions [75]. From this point of view, the sintered porous structure should be considered as particles connected by necks, the size and amount of which change with the heating process, affecting diffusion mass phenomena. Therefore, its λ_{eff} depends on the number of created necks. The microstructural investigation is the starting point to modelling heat conductivity for a porous sintered NiAl material based on the real structure.

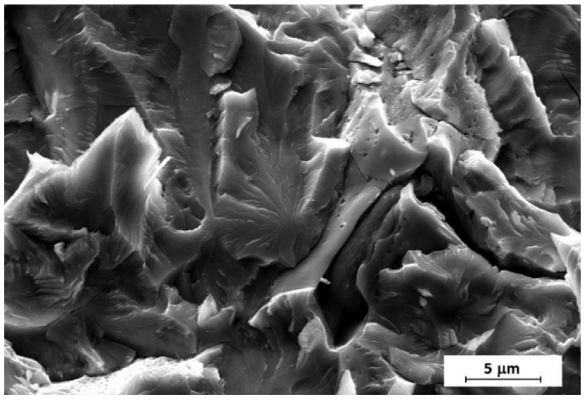

Fig. 7. SEM image of the fracture of almost fully dense NiAl material (sample 6 -T_s=1100°C, p=30 MPa, d_{rel}=97.5%).

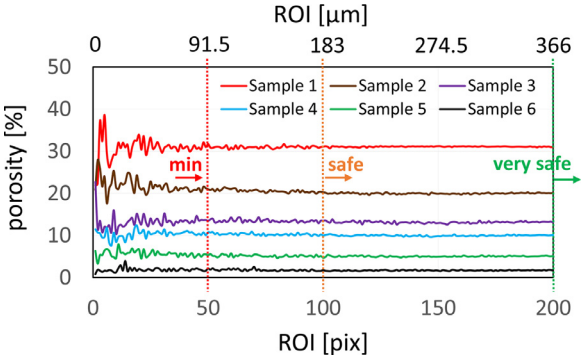

Fig. 8. Porosity as a function of the region of interest (ROI) size.

3.1.2. Quantitative analysis

Sintered NiAl samples have been investigated quantitatively in the context of several microstructural parameters. In the first stage of the quantitative analysis of the microstructure of porous samples, the homogeneity of the volume fraction of phases (i.e., NiAl and pores) was investigated considering the size of the ROI (Fig. 8).

Table 1
Summary of microstructural and thermal properties of sintered NiAl samples.

	No. (sintering temp., pressure)	Sample 1 (1100°C,5MPa)	Sample 2 (1200°C,5MPa)	Sample 3 (1300°C,5MPa)	Sample 4 (1100°C,30MPa)	Sample 5 (1200°C,30MPa)	Sample 6 (1300°C,30MPa)
Experimental	**relative density [%], d_{rel}**	70.2	78.2	84.4	89.3	95.0	97.5
	porosity [%]	29.8	21.8	15.6	10.7	5.0	2.5
	effective thermal conductivity [W/mK], λ_{exp}	33.5± 2.3	47.3±2.4	52.5±1.7	68.2±2.0	76.1±1.8	83.4±3.3
Quantitative analysis	**specific surface area [1/μm]**	0.109	0.089	0.065	0.055	0.038	0.019
	open porosity [%]	30.40	19.53	11.52	6.75	2.23	0.73
	closed porosity [%]	0.59	1.02	1.70	3.39	2.97	1.01
	mean pores size [μm]	11.07	11.54	12.02	12.43	10.38	11.86
	degree of anisotropy	1.17	1.18	1.51	1.25	1.18	2.23

Thus, the volume fraction of pores (porosity) was analysed for smaller 3D images randomly extracted from the large, original image, obtained by micro-tomography. For each ROI size, 10 images were used to calculate the average porosity.

The results presented in Fig. 8 indicate that all the materials studied are relatively homogenous where porosity is concerned. This suggests that the representative size of the region of interest can be reduced to a minimum of 50 × 50 × 50 pixels (voxels), where the average porosity converges to a specific value with low variation. In numerical simulations, a reduction in the size of the ROI is often a compromise between accuracy of results and calculation time. Based on the above results, the size of the systems for numerical analysis was set as 100 × 100 × 100 for more advanced simulations and 200 × 200 × 200 when less demanding calculations were required.

Quantitative 3D image analysis was performed on 200 × 200 × 200 voxels. Each analysis was repeated for ten randomly-extracted regions from the original, large micro-tomography image. The analysis was performed using the Avizo and SkyScan CT analyser CTAn software. The Otsu algorithm was utilised for the automatic thresholding procedure. Global and local microstructure parameters were characterised as follows:

- open/closed porosity – measured as the ratio of the number of voxels representing open/closed pore space to the total number of voxels in the ROI,
- mean pore size – obtained by inscribing spheres into pore spaces and calculating the mean diameter value,
- specific surface area – calculated as the ratio of the surface of solid phase to the total ROI volume,
- degree of anisotropy (DoA) – is calculated using mean intercept length (MIL) and Eigen analysis. Firstly, MIL is calculated for the large number of random 3D angles. Next, the polar plot of MIL vectors is generated and an ellipsoid is fitted to this plot with tensor representation. Finally, DoA is measured as a ratio of maximum eigenvalue to the minimum eigenvalue of the tensor representing the ellipsoid.

The results of quantitative image analysis are shown in Table 1, along with relative density and λ_{eff} which have been measured experimentally. It can be observed that the total porosities measured experimentally and calculated from image analysis of X-ray CT images differ slightly; the lower the absolute value of porosity, the higher the difference.

The results clearly indicate that higher sintering temperature and pressure lead to lower total porosity (open + closed) and a higher relative density of materials studied herein. On the other hand, it can also be observed that the average pore size does not change significantly (minimum 10.38 μm, maximum 12.43 μm).

3.2. Simulation and modelling results

3.2.1. General overview

Extensive numerical analysis of heat transfer of sintered samples was carried out based on the methodology presented in section 2. Six geometrical models representing NiAl samples with different porosities, obtained from the micro-CT analysis, have been used in finite element simulations to evaluate λ_{eff} and its dependence on the structural and thermal features. Macroscopic (volume fraction of samples, λ_{eff}, tortuosity) and microscopic quantities (magnitudes of heat fluxes q and deviation angle $\boldsymbol{\beta}$, presented as average value with standard deviation) are presented in Table 2. The effect of sintering process parameters (temperature and applied pressure) and the relative density and porosity on the simulation results have been studied and discussed in further subsections (3.2.2 to 3.2.5).

3.2.2. Heat fluxes analysis

With the real representation of porous samples determined via micro-CT imaging, it is possible to characterise the local thermal effects of sintered NiAl materials. Fig. 9 presents the graphical distribution of heat flux magnitudes (q) of six studied samples. As can be observed, the spatial distribution of q depends closely on structural features such as particle size and shape, the number and size of particles/necks, and porosity characteristics. Microstructural and quantitative analyses (section 3.1) reveal a considerable difference in sample design, which affects the heat transfer performance substantially. The samples with higher porosity, i.e., those manufactured with assistance of lower external pressure (samples 1–3 in Figs. 9a–c), are characterised by smaller-sized, bottleneck-shaped necks connecting powder particles with narrow channels for heat flow. Limited and undeveloped necks effectively constrain the heat flow. Hence, such locations (being in parallel to prescribed heat flow) indicate maximized values of q. On the other hand, such samples demonstrate lower local heat flux in regions within the volume of the largest particles and in the interfacial area of solid-pore elements, channelled perpendicular to the prescribed heat flow. More discussion on the aforementioned effect follows in sections 3.2.4 and 3.2.5.

More privileged sintering conditions with higher external pressure and/or sintering temperature provide a higher number of advanced-sized cohesive bonds with simultaneous grain/particle growth, and a reduction of pores and voids (samples 4–6 in Figs. 9d–f). Having large channels and streamlined paths to heat flow, the sparse heterogeneities of heat fluxes (red and blue colour) are placed in the pore locations. Maximum values can be observed in the solid-pore interface in the direction parallel to heat flow and the minimum ones observed in the perpendicular direction.

Table 2
Summary of properties of sintered samples evaluated by FEM simulations.

No. (sintering temp,pressure)	Sample 1 (1100°C,5MPa)	Sample 2 (1200°C,5MPa)	Sample 3 (1300°C,5MPa)	Sample 4 (1100°C,30MPa)	Sample 5 (1200°C,30MPa)	Sample 6 (1300°C,30MPa)
relative density of FE samples [%], d_{rel}	70.2	78.2	84.4	89.3	95.0	97.5
effective thermal conductivity, λ_{eff} [W/mK]	45.2	55.8	66.4	75.7	79.2	84.1
average magnit. of heat flux q with stand. dev. [kW/m^2]	34.5±14.1	40.3±11.6	43.2±9.5	45.7±7.1	46.5±5.9	47.5±4.0
average deviation angle of heat flux β with stand. dev. [°]	18.3±15.4	13.9±12.4	10.7±10.7	7.1±8.5	5.4±7.0	2.9±4.7
thermal tortuosity – analytical rel.	1.184	1.096	1.054	1.032	1.016	1.006
thermal phenom. tortuosity, τ_t with stand. dev.	1.130±0.100	1.073±0.038	1.040±0.028	1.017±0.018	1.010±0.019	1.002±0.010
geometrical tortuosity, τ_g with stand. dev.	1.210±0.113	1.134±0.069	1.090±0.054	1.052±0.047	1.033±0.031	1.013±0.032

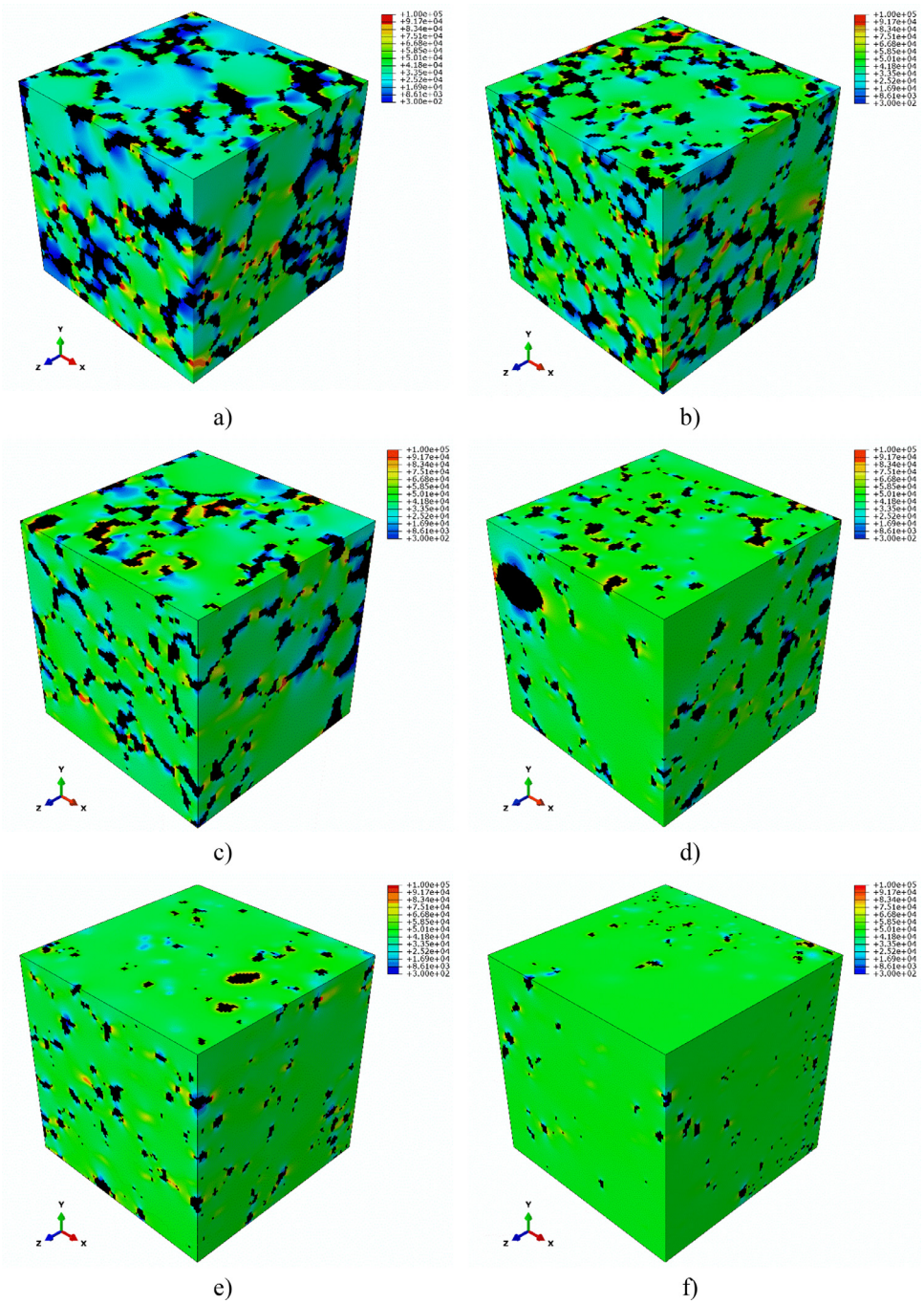

Fig. 9. Graphical distribution of heat fluxes magnitudes q in: a) sample 1 (d_{rel}=70.2%), b) sample 2 (d_{rel}=78.8%), c) sample 3 (d_{rel}=84.4%), d) sample 4 (d_{rel}=89.3%), c) sample 5 (d_{rel}=95%) and d) sample 6 (d_{rel}=97.5%).

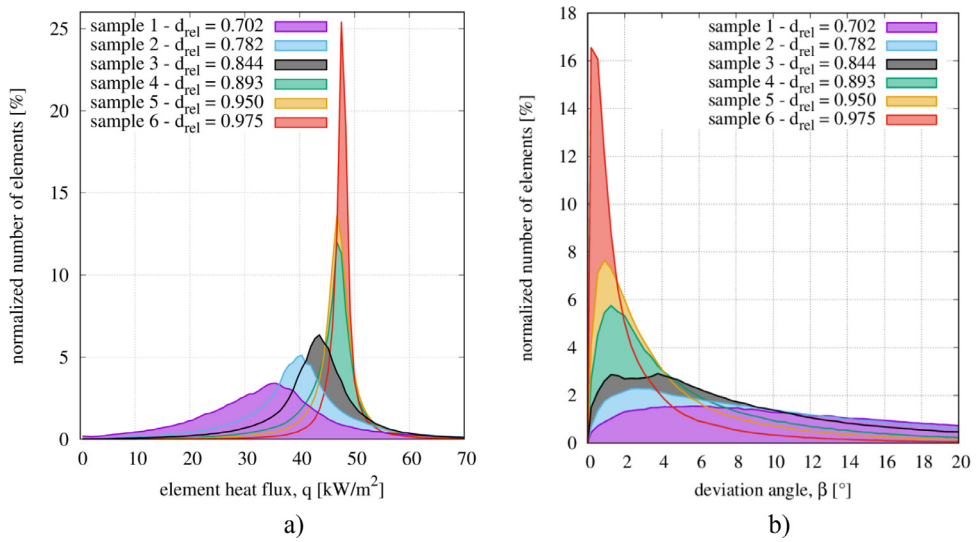

Fig. 10. The distributions of: a) element heat fluxes (magnitude), b) deviation angles from prescribed direction of heat flux (the central axis of flow) for NiAl samples.

The heterogeneity of q for the most porous samples has been explicitly confirmed in the distributions shown in Fig. 10a. It was proven that widespread heat fluxes are strongly connected with a lower relative density in a sample. The more complex and non-trivial structure of porous samples results in a relatively low average q with a sizeable standard deviation, which evolves with decreasing relative density (Table 2).

Besides the clear impact of the distribution of heat flux magnitudes, porosity changes the direction of $\vec{q}$ vectors with respect to the central flow axis. In order to measure the directional variation of the $\vec{q}$ vector, the deviation angle β has been introduced (Fig. 3). The distribution of the parameter for six samples is shown in Fig. 10b. The distribution character and the average value of deviation angles varies significantly for different porosities. Similar to the distribution of heat flux magnitudes, Fig. 10b reveals the heterogeneous spread for less dense samples and a more compacted and homogenous spread for samples with higher density. The larger number of pores and voids is apparent in samples 1–3, forced to deflect the heat fluxes from the prescribed direction of flow as they approach the physical obstacle.

3.2.3. Tortuosity

The investigated deviation angles of heat fluxes vectors β, presented in Fig. 10b are strictly related to the tortuosity of local heat flow and, hence, to the macroscopic (average) tortuosity, being one of the main microstructural factors of porous materials. As a consequence, all sintered samples have been analysed in terms of the streamlined level of path/flow, evaluated by geometrical and thermal phenomenological models as discussed in section 2.2.4. Fig. 11a shows the graphical representation of curves within the volume of sample 1.

It can be clearly seen the considerable spread of curve shapes originates from a large number of flow obstacles in the form of elements corresponding to pores and voids. The effect of tortuous flow is shown in Fig. 11b, where the representative curves with deviation distance (measured by unit element size) from the axis of prescribed flow are designated by the top starting element. As the tortuosity increases, the curves indicate more complex shapes with greater deviation distances elongating in this way, with the effective route from top-to-bottom surfaces of the sample calculated via L_g parameter (Eq. (10)).

The impact of sample density on local tortuosity parameters is presented in Fig. 12. The proposed distributions reveal a high dependence between each sample, regardless of evaluation methodology. Samples manufactured with the assistance of higher pressure, i.e., higher density, are characterised by the prevalence of flows closer to 1, with maximum values of 1.3 for geometrical tortuosity and 1.2 for thermal phenomenological tortuosity. Lower pressure during SPS results in higher porosity and a significantly hindered path for heat flow, which can be observed as a wide spread of tortuosity results (up to 1.6 for geometrical tortuosity). When comparing the geometrical and thermal distributions, it should be noted that the thermal distribution is more compact, showing that the path can be lowered by the approach predicated on heat fluxes.

A more relevant comparison was made of the performance of different tortuosity evaluation methods and is shown in Fig. 13. The graph shows the average value of geometrical and thermal phenomenological tortuosities from more than 100 flows, with additional results from the thermal approach based on the analytical relation (Eq. (11)). In all three cases, the density growth is associated with lower tortuosity; thus, all methods show a similar and valid trend. On the one hand, these results show a certain discrepancy between each technique; on the other hand, a satisfactory coincidence can be observed compared to the analogical study of a different kind of tortuosity described elsewhere [4].

The highest value for all sintered samples was obtained via the geometrical approach. It should be noted that the path is realised by a zig-zag pattern, passing the pores through many constrictions and bottlenecks of solid material channels. This makes the geometrical tortuosity a microstructural characteristic, independent from the specific transport process in porous media [76]. In contrast to thermal approaches, the geometrical method simply bypasses obstacles via a search algorithm of first-order neighbours, and does not take advantage of the heat flow as a guideline to predict the path (Fig. 3). Such a feature allows the thermal methods to lower the effective path by smoothing the flow deflection before contact with void elements much sooner. Finally, it should be mentioned that, based on analytical results, the thermal phenomenological model lowers the effective path more than the thermal model by application of special smoothing procedure, allowing aversion of the flow variation in the cross-section of channels of solid material elements. Certainly, the effect of flow variation is considered in

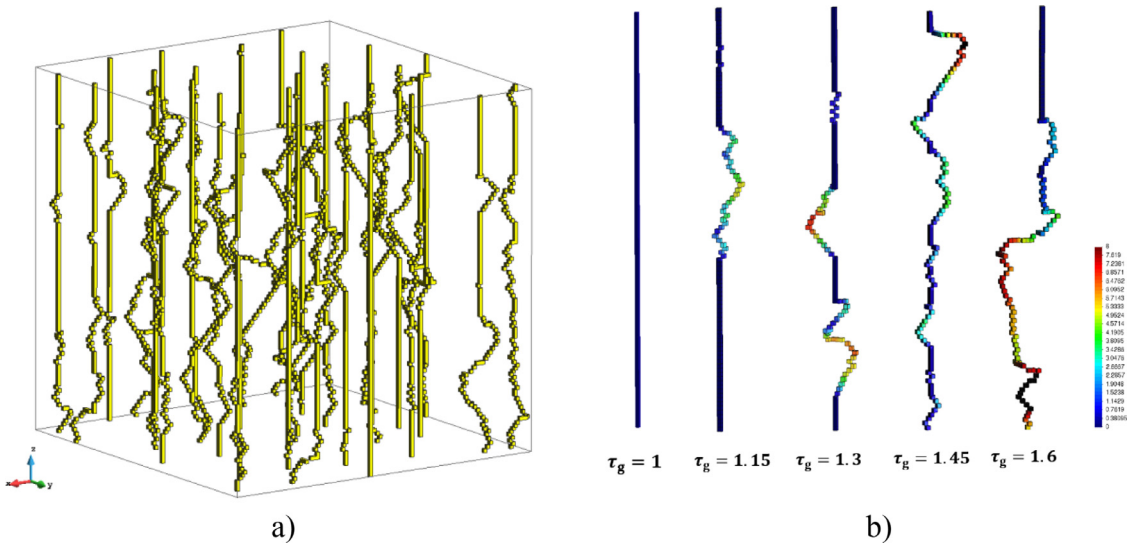

Fig. 11. Overview of tortuosity analysis. Collection of 30 representative curves within sample 1 (a), representative tortuosity curves with deviation distance (measured by unit element size) from the central axis of flow designated by top starting element (b).

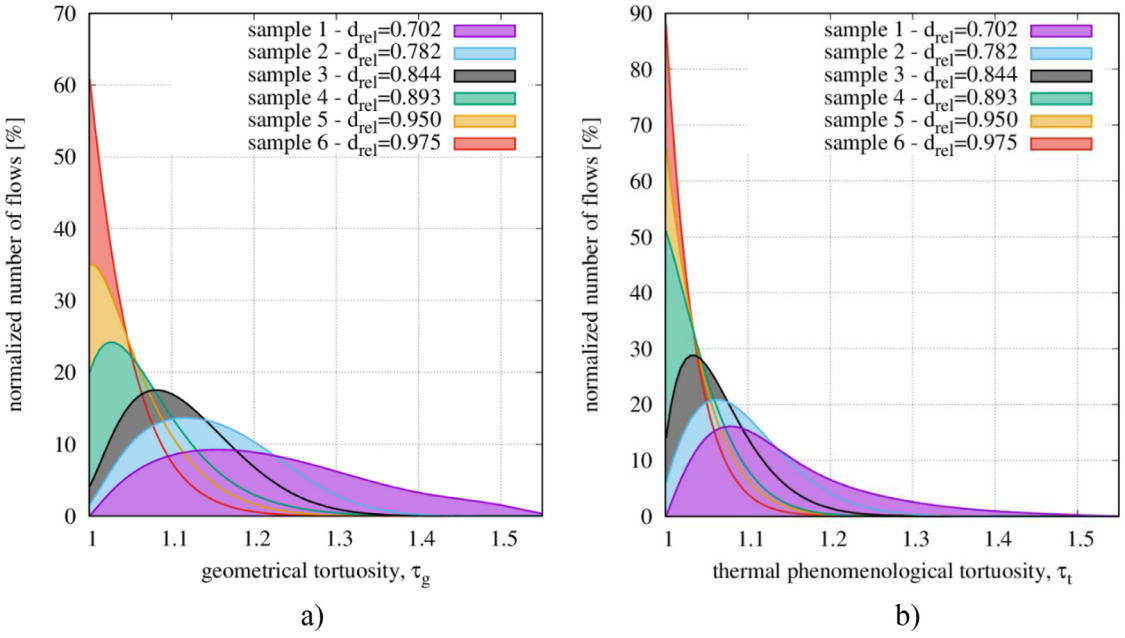

Fig. 12. The tortuosity distributions of: a) geometrical and b) thermal phenomenological approaches for samples with various densities.

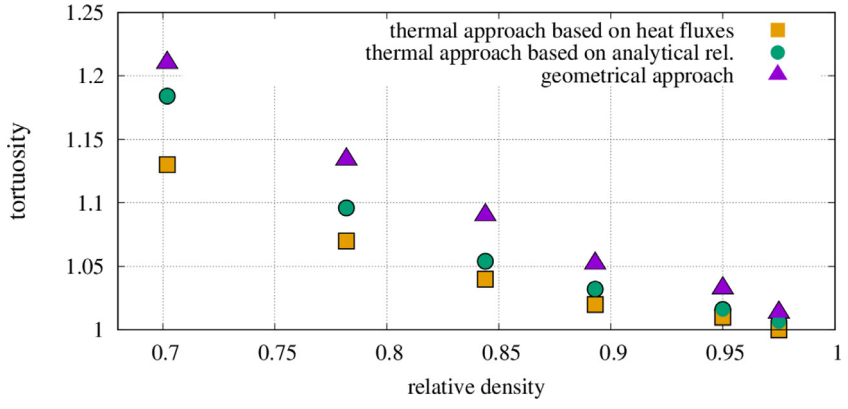

Fig. 13. The summary of thermal analytical, thermal phenomenological and geometrical tortuosity of NiAl samples with various density degree.

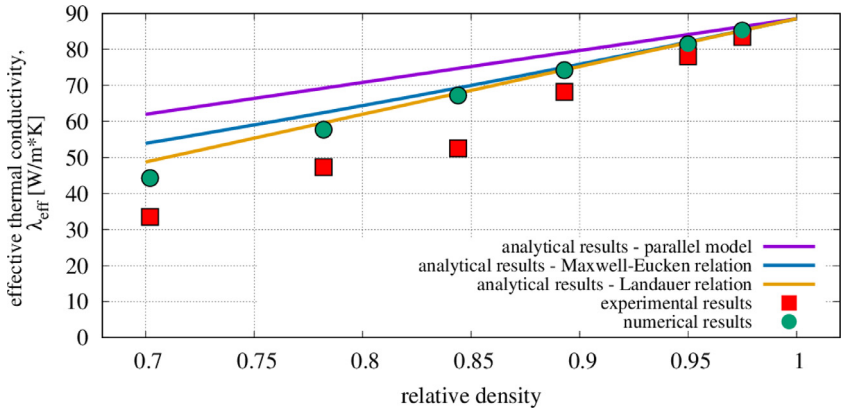

Fig. 14. The summary of analytical (parallel, Maxwell-Eucken and Landauer model), experimental and numerical FEM results of effective thermal conductivity of NiAl samples with various relative densities.

the heat transfer simulation, which is the foundation of the determination of λ_{eff}, this being the input parameter in Eq. (11). Hence, the thermal tortuosity based on the analytical relation may overestimate the results compared to the phenomenological model.

3.2.4. Validation of numerical and analytical results

One of the major purposes of finite element simulation was to validate the numerical results of λ_{eff} evaluated utilising the procedure presented in section 2.2.3. Determined values for λ_{eff} have been compared with corresponding experimental results (Table 1) and analytical results (discussed in section 2.2.2). Fig. 14 presents a summary of experimental and analytical results for λ_{exp} (parallel, Eq. (6); Maxwell-Eucken, Eq. (7); and Landauer, Eq. (8)) and numerical results as a function of relative density. Input parameters of analytical models, namely thermal conductivities of the solid, λ_s and pores, λ_p, have been set similarly as in FE simulations.

The first impression of the comparison of effective thermal conductivities is the considerable disagreement of experimental and analytical datasets. The highest deviation can be observed for the parallel model. As the analytical relationship appears to be more complex and sophisticated (Maxwell-Eucken and Landauer), the theoretical results better represent the experimental behaviour. On the other hand, the Landauer relation corresponds well with finite element results over approximately the entire studied range of relative densities. This can be explained by its theoretical background, and several physical assumptions lie behind it – in particular, a random distribution of open porosity within the investigated domain. Such structural features can be easily compared with geometrical models based on micro-CT, indicating a serious resemblance as shown in quantitative analysis of NiAl samples (section 3.1.2).

Despite such similarities, both numerical and analytical results for higher-porosity samples deviate significantly from experimental data. Fig. 14 shows that thermal conductivities calculated by FEM and the Landauer model are overestimated. Both approaches predict a change in λ_{eff} due only to porosity evolution, without any microscopic effects affected by the manufacturing process. In particular, FEM and Landauer models do not consider the ITR explicitly as the effect reducing the heat conduction in a porous polycrystalline material.

In the case of sintered material with a high degree of porosity, the bonding of powder particles in the form of necks forms the structural spots blocking heat flow. As discussed in section 3.1.1, in sintered systems thermal resistance can occur due to both thermal contact and boundary resistance to varying degrees and due to different sintering conditions [13]. The samples manufactured with limited external pressure (samples 1–3) may generally demonstrate imperfect particle-particle contacts at the microscale, despite the application of relatively high sintering temperatures (sample 3). On the other hand, the intense powder compaction resulting from higher external pressure supports the development of bonding through multiple contact points along the neck area. However, a qualitative connection between neighbouring particles cannot be ensured due to the low sintering temperature (sample 4). Analysis of samples 5 and 6 shows that only the application of relevant loading to the powder mixture and providence of relatively high sintering temperature guarantees the intensified mass transport via diffusion mechanism and, thus, produces fine particle-particle bonding with similar thermal conductivity to crystalline materials.

As a consequence, the thermal interfacial resistance of necks appears to be an essential subject in heat conduction through nearly-sintered porous media. In fact, by neglecting this material's effect and assuming perfect thermal conductivity through the necks, we consequently over-predict effective thermal conductivities [41]. Accurate predictions of λ_{eff} require a precise investigation of the interfacial heat transport [48].

3.3. Consideration of interfacial thermal resistance

3.3.1. Finite element framework

To express the importance of analysis of heat conduction through the necks, we consider the additional thermal resistance located in the cohesive bonding between particles of the NiAl sample and its effect on macroscopic behaviour. The thermal resistance of necks can be represented within the finite element framework as the third autonomous "phase" (named as *resistance phase*) in the volume of the sintered sample, similar to previous reports [41,48]. An auxiliary phase should indicate a lowered value of thermal conductivity due to the structural nature of necks. However, three aspects of numerical investigation should be addressed, specifically the fraction υ_r, the thermal conductivity of resistance phase elements λ_r, and their spatial location within the finite element model.

Due to the X-ray testing nature and employed methodology, the micro-CT analysis does not allow us to distinguish individual particles or grains, nor to localise their contact points. Hence, it treats the solid phase as the continuum body, as opposed to several experimental (e.g., electron backscatter diffraction [77]), analytical [13,48] and micromechanical particle approaches [25,26,48,78]. In order to highlight the necks within the geometrical micro-CT model, a special generation algorithm has been adopted. Its foundation comes from the idea that the necks, considered as reduced-sized channels for heat conduction, are the regions with the maximum local q, as discussed in section 3.2.2 and shown in Fig. 15.

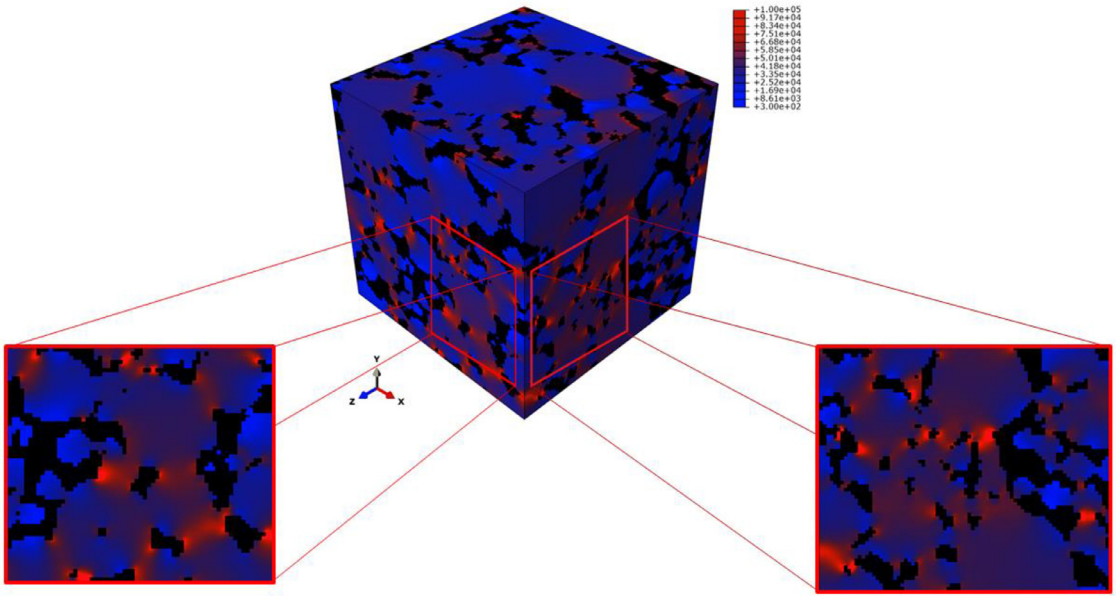

Fig. 15. The graphical distribution of maximum magnitudes of heat fluxes q of sample 1 after heat transfer simulation along y direction.

Therefore, it can be clearly seen that the bonding of particles are characterised by a maximised q in contrast to particle centres.

Taking advantage of the aforementioned effect, we develop the generation algorithm of the resistance phase with the following assumptions:

- finite elements designated as the resistance phase are appointed from *generation simulation* performed in three orthogonal directions to capture the necks oriented differently to the prescribed heat flow direction,
- the main indicator of designation of resistance phase is the value of local q in the prescribed heat flow direction,
- a certain number of assigned finite elements n_r exhibiting the maximum heat flux value is selected and converted from solid to resistance phase,
- in order to perform the generation simulation while the resistance phase is already present at a level $\upsilon_r = n_r/n_{total}$, the value of thermal conductivity of the resistance phase, λ_r, is set as $\lambda_r/\lambda_s = 80\%$. The proposed value has been established in a number of tests assessing the performance of the generation algorithm, ensuring the best possible location of the resistance phase within particle necks,
- as the spots are filled with a new phase, the algorithm controls the number or resistance phase elements in each layer of the sample, n_r^i (i = layer number), and generates a homogeneous distribution along the whole sample in a given direction.

The capability of the generation algorithm can be reviewed on the basis of generated structures varying the content of the resistance phase (Fig. 16). Essentially, the proposed algorithm placed the new elements with lower thermal conductivity within the geometrical constrictions of the solid phase related to the bonding of powder particles. As υ_r increases, the new locations are distinguished and new necks are covered by the resistance phase. Although the generation method shows relatively competent performance, it also reveals two main deficiencies. Firstly, despite the considerable resistance phase content ($\upsilon_r = 20\%$), scarce locations are still not filled by new elements. Secondly, instead of covering the prompting spots, the new elements of the resistance phase agglomerate within the area of existing particle boundaries; hence, creating "clusters". Nonetheless, the application of the optimisation procedure ensures a homogenous distribution of the number of resistance phase elements in each layer n_r^i, minimising the observed agglomeration effect, as shown in Fig. 17. The parameter n_r^i deviates slightly along the layers due to the local microstructural features (e.g., local porosity, grain size), ultimately keeping the parameter close to the prescribed value (400 for $\upsilon_r = 4\%$).

Keeping both the advantages and drawbacks of the proposed method in mind, the performance of the generation algorithm has been verified by a simple benchmark consisting of its comparison with a corresponding sample with a random distribution of resistance phases. Several finite element simulations of heat conduction have been performed for two types of samples (generated by an algorithm or randomly) with various fractions of υ_r (0 to 20%) and ratio $\lambda_r/\lambda_s = 0$. The measure of the effectiveness of the proposed test is the reduction rate of λ_{eff}. As the drop in λ_{eff} becomes more pronounced and macroscopic resistance is stronger, the generation method locates the elements of the resistance phase in sensitive and critical spots, referring to particle necks. The comparison of the effectiveness of the generation algorithm is presented in Fig. 18. The reduction rate of the proposed new method is significant with respect to the random one, demonstrating a linear decrease of λ_{eff} along with an increase in the fraction of resistance phase similarly to porosity growth. The generation algorithm offers the high limiting of heat conduction by reducing λ_{eff}, down to nearly 0 W/mK for $\upsilon_r = 20\%$.

The reduction in λ_{eff} has its origin in the characteristic of heat conduction through porous samples on the microscopic scale. As discussed in section 3.2.2, the distributions of each element's q and the deviation angles for modified sample 1 ($\lambda_r/\lambda_s = 0$) with different resistance phase fractions are analysed in Figs. 19a and b, respectively. In accordance with expectations, the addition of the resistance phase, intended to serve as ITR, effectively blocks the flow by decreasing q locally (Fig. 19a) in the vicinity of dissipative phases (such porosity and/or the resistance phase) while simultaneously deviating the flow by frequently increasing the angles from the prescribed direction higher than 90° (Fig. 19b).

A further and more detailed investigation of the dependence of ITR on λ_{eff} is shown in Fig. 20. Analogically to the previous benchmark example, samples with variable resistance phase fractions were generated in intervals of 2% for υ_r, up to 10%, and then in intervals of 5% up to 20%. The different ratios of λ_r/λ_s were studied, from 0 to 70% for graphs and from 0 to 100% for heat maps.

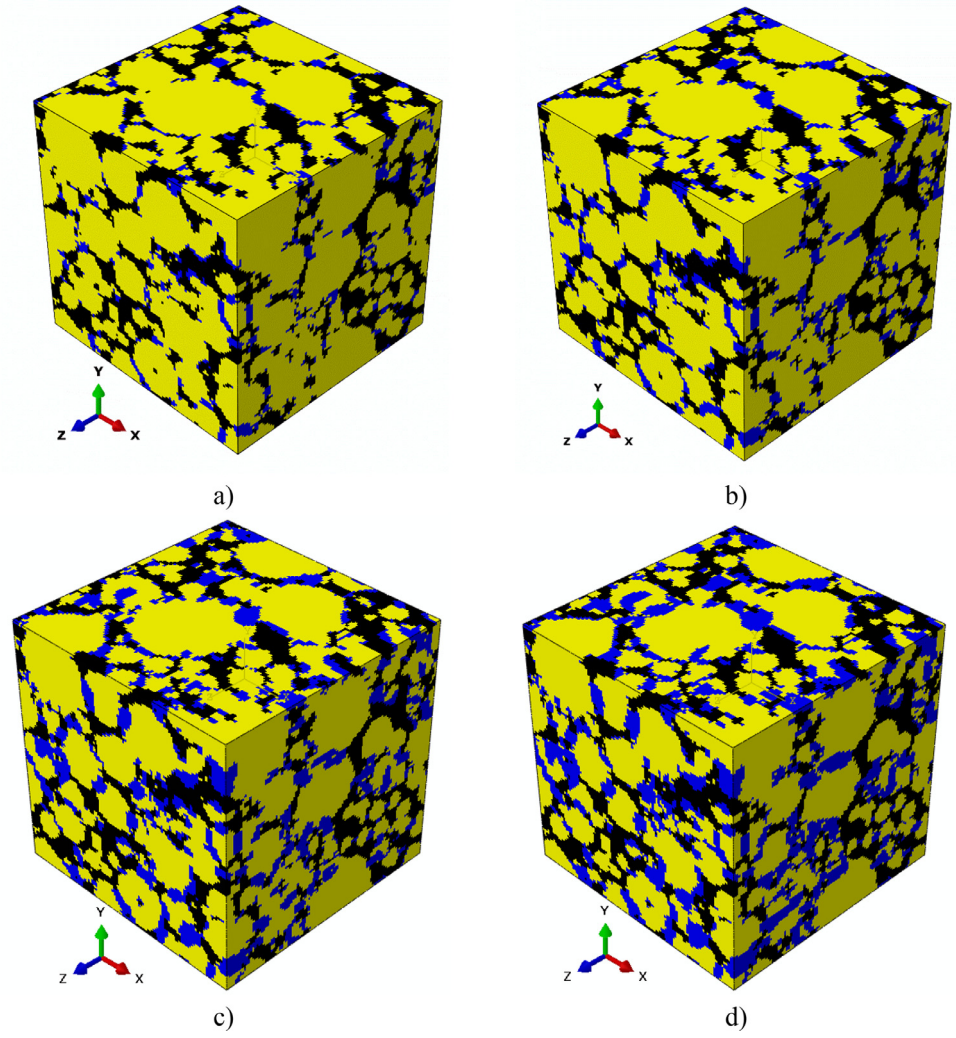

Fig. 16. Microstructures of modified sample 1 containing: a) $\upsilon_r = 6\%$, b) $\upsilon_r = 10\%$, c) $\upsilon_r = 15\%$ and d) $\upsilon_r = 20\%$ of resistance phase (blue color).

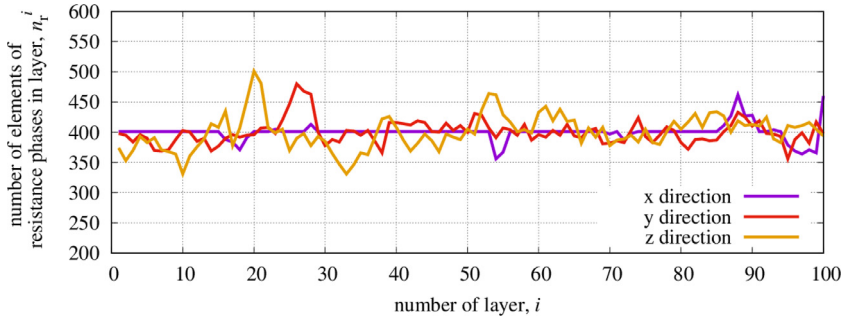

Fig. 17. Distribution of resistance phase within each layer along three orthogonal directions for sample 1 with $\upsilon_r = 4\%$. Total number of elements in each layer = 10000.

Points marked on the graphs denote λ_{eff} results calculated from FE simulations, and lines show the approximation of FE results. Finite element investigation of interfacial thermal resistance and λ_{eff} has been performed for samples with the highest porosities, i.e., samples 1-4, as the need to address the resistance at the necks is highest due to serious disagreement with experimental data (Fig. 14).

Essentially, as λ_r/λ_s is close to 100%, the ITR demonstrates no impact on λ_{eff}; thus, there is no difference in the rate of thermal energy transferred through either the solid (particle) or neck. Assuming a λ_r/λ_s ratio lower than 100%, we expect to reduce the macroscopic behaviour of heat conduction by disturbing the local heat transfer via particle bonding, considered the critical location of energy flow. In an extreme case, by setting the ratio $\lambda_r/\lambda_s = 0$, we declare that the generated resistance phase has no thermal conductivity and can be treated in the same way as porosity.

For samples 1 and 2 (Figs. 20a and b) especially, by decreasing the λ_r/λ_s ratio we notice that λ_{eff} is limited more rapidly with the non-linear matter by hindering thermal energy in the boundaries among particles, and heat is mainly transferred through the solid part [41]. The increase of resistance phase fraction results in a considerable drop in λ_{eff}. As υ_r increases the λ_{eff} decrease occurs at a lower rate, due to approaching zero conductivity and to

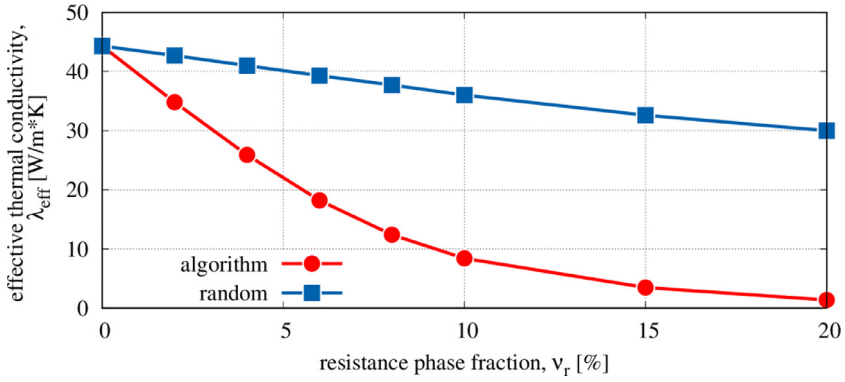

Fig. 18. Effective thermal conductivity vs. fraction of resistance phase for various generation approaches.

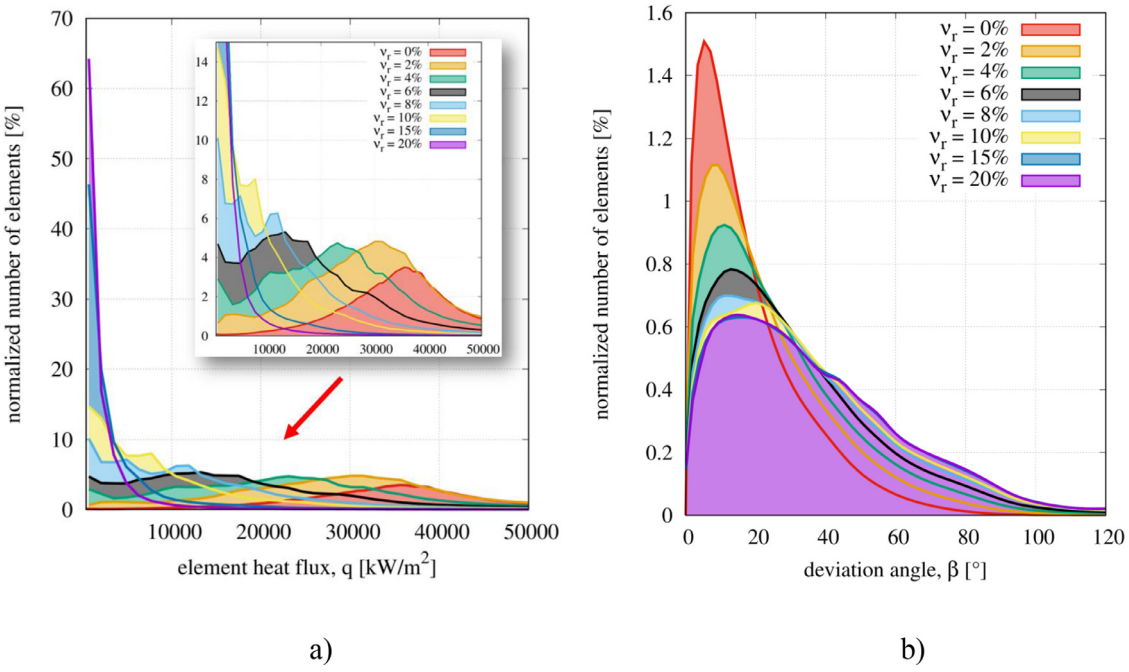

Fig. 19. The distributions of: a) element heat fluxes (magnitude), b) deviation angles for samples 1 with different resistance phase fractions.

the clustering effect of resistance phase elements within the sample, among other causes. Samples 3 and 4 (with lower porosity, Figs. 20c and d) show a more linear dependence, regardless of applied λ_r/λ_s ratio.

In order to study the agreement of obtained FEM results with experimental data, the experimental thermal conductivity (λ_{exp}) has been inserted in each graph. To avoid the uncertainties in experimental data for each specific measurement point (Table 1), the linear approximation of λ_{exp} has been used. As the curves for various values of λ_r/λ_s cross the experimental line (Fig. 20), agreement for each sample has been observed. Moreover, the ratio of λ_{eff} determined by FEM and experimentally ($\lambda_{eff}/\lambda_{exp}$) was introduced.

The dimensionless parameter has been utilised in heat maps with the identification of the experimental zone corresponding to the standard deviation of thermal conductivity measurements (Table 1). In other words, the experimental zone with $\lambda_{eff}/\lambda_{exp}$ ratio close to 1 shows the combination of FEM simulation parameters, λ_r/λ_s ratio and υ_r, ensuring consistency between numerical and experimental results.

As can be observed for all samples studied, agreement between experimental and numerical results, reflected in the presence of the experimental zone, has been found. Four heat maps corresponding to four samples each reveal relatively similar behaviour within the presented parametric study. The experimental zone increases non-linearly with increasing λ_r/λ_s and υ_r. The increase of the position of the experimental zone appears to be more evident as density increases (highest for sample 4 and lowest for sample 1). The correspondence of numerical and experimental results demonstrated in the experimental zone for sample 4 should be easier to achieve (for higher λ_r/λ_s ratio) due to the expected better physical state of cohesive bonding, resulting primarily from application of higher external pressure and secondarily from minor differences with experimental data. Furthermore, by keeping the same range of $\lambda_{eff}/\lambda_{exp}$ along with the four heat maps, a higher deviation of the dimensionless parameter can be observed as the porosity rises both from the upper side (red) and bottom side (blue) of the experimental zone.

3.3.2. Analytical modeling

The validation of analytical and experimental data of λ_{eff} for samples with different densities brought failure regarding agreement of results (Fig. 14). Three of the studied models – parallel, Maxwell-Eucken and Landauer – were unable to represent the macroscopic thermal behaviour of sintered materials correctly, without consideration of ITR effect. The proposed new finite element model with an introduced resistance phase confirms the re-

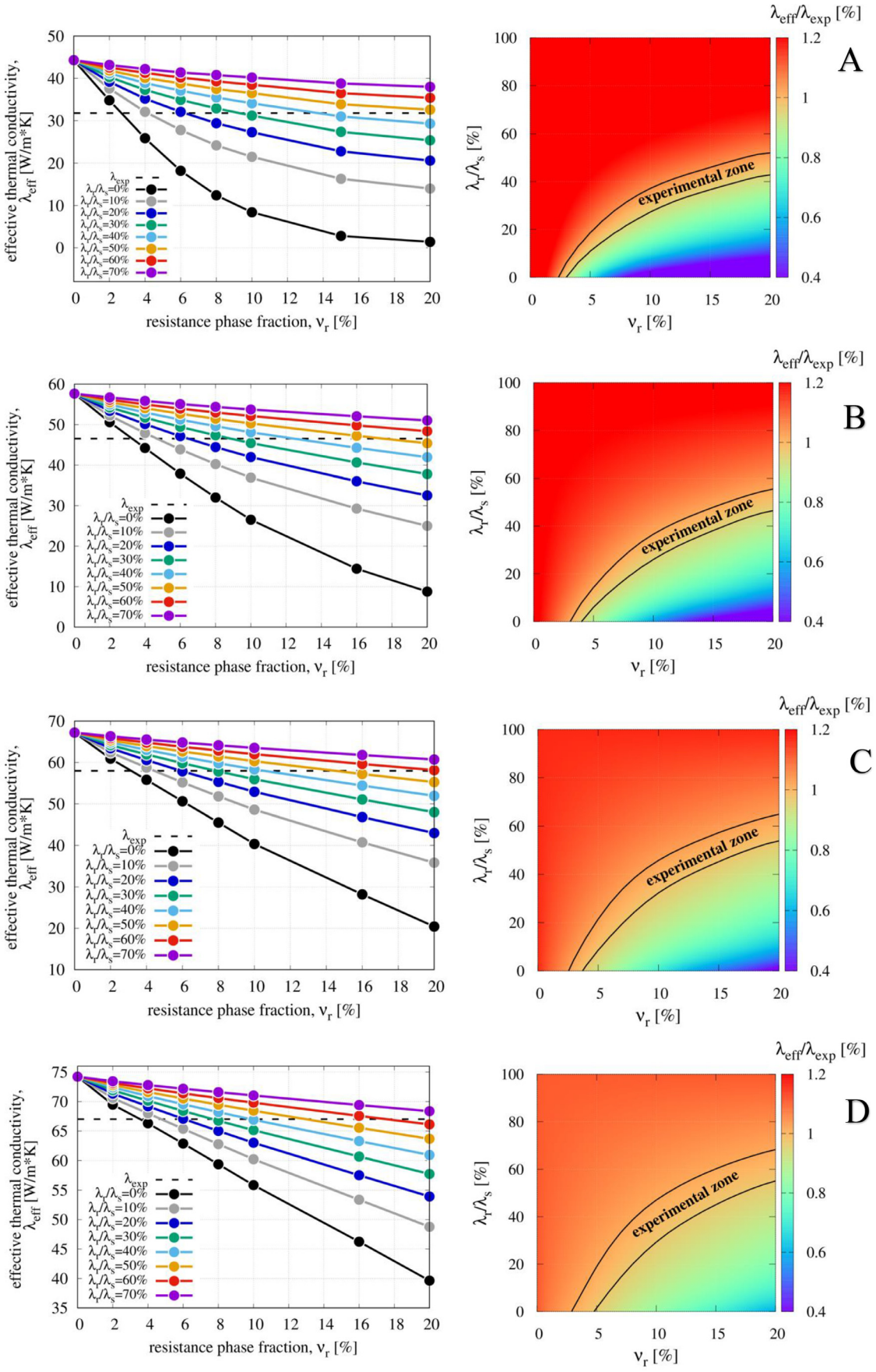

Fig. 20. Graphs (left side) and heat maps (right side) of effective thermal conductivities in function of resistance phase fraction for various λ_r/λ_s ratio with its coincidence with experimental results of sample 1 (A), 2 (B), 3 (C) and 4 (D).

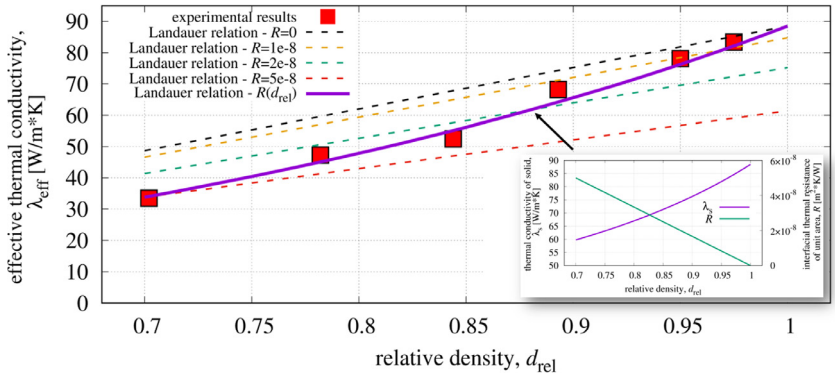

Fig. 21. Modification of analytical Landauer model with consideration of interfacial thermal resistance and its agreement with experimental results of thermal conductivity.

quirement for the application of the dissipation mechanism related to particle contacts/boundaries, and, hence, the achievement of the best possible correspondence with experimental results of λ_{exp}.

In order to take the ITR into account within the analytical modelling, the Landauer model, which represents the experimental data better than the other two studied relations, has been modified by including the resistance in the form of the Yang model (Eq. (4)). In a similar manner, using the brick layer model, the Landauer relation has been efficiently used to predict λ_{eff} of alumina samples with various pore volume fractions manufactured in different firing conditions [39], using a constant value of grain boundary thermal resistance (per unit area) *R*. Such assumptions have been tested in our investigation and are presented in Fig. 21. Averaged grain size (d_{avg}), summarised for all samples, has been estimated as 9.2 μm based on micro-CT investigation of starting powders. Such assumption is justified since the spark plasma sintering significantly limits the grain growth during the densification process. The thermal conductivity of pores (λ_p) has been kept the same as in previous tests, while the thermal conductivity of the crystal (λ_c) has been set as 88.5 W/mK, as per the fully-dense dense material.

Several curves representing analytical results for λ_{eff}, obtained by the application of a number of constant *R* values has been compared to experimental data. Despite the Landauer model's success for fired alumina samples with a constant value of *R* for different porosity, it fails for sintered NiAl samples. This can be explained by the fact that as the SPS condition of our samples differs, affecting the microstructure diversely at microscopic (i.e., size and quality of particle contacts), keeping the same value of *R* seems to be unrealistic and too simplistic an assumption. As discussed in sections 3.1.1 and 3.2.4, the application of higher external pressure and/or sintering temperature should improve heat transfer through the necks significantly, and simultaneously reduce the ITR.

In view of the above, the thermal resistance through particle contacts has been approximated by a linear relation as a function of relative density. Since there is no literature data regarding the ITR of NiAl grain boundaries (or necks), and literature is limited for other metals, R_{max} has been calibrated to fit the value of λ_{exp} for sample 1. The proposed range of R - $R_{max} = 5 \times 10^{-8}$ $m^2/(K \bullet W)$ for $d_{rel} = 0.7$; $R_{min} = 0$ $m^2/(K \bullet W)$ for a fully-dense sample, presented in Fig. 21 as a miniature graph) corresponds with data found in the literature regarding the Kapitza resistance results for lowly-conducting grain boundaries [18,39,48]. However, it should be noted that cited references specify the R values of ceramics mostly, such as alumina, in which the main mechanism of heat conduction is lattice vibrations and hence, it may indicate a quite different characteristic compared to the movement of the electrons being the dominant carrier of thermal conduction in the intermetallic compounds [37]. Due to the lack of literature data, the value of R_{max} cannot be verified more, however assumed considerable resistance seems to be realistic considering the neck structure of sample 1 (Fig.5a). The material structure at this state should be treated as the starting point of sintering. Because of the insufficient sintering temperature, practically no initial compression and reduced sintering time, bonding between individual particles is very weak and the macroscopic stability of the sample is highly frail. Along with thermal boundary resistance of limited size necks, the very early stage of sintering is accompanied by the thermal contact resistance, which dissipates the heat flow very effectively [41].

The miniature graph in Fig. 21 also shows the nonlinear evolution of thermal conductivity of the solid (λ_s) as the effect of the decay of ITR. As stated previously [18], *R* decreases for higher temperature treatments (along with extra powder loading), suggesting that the more resistive higher-energy grain boundaries are eliminated as sintering progresses accompanied by the neck formation with a considerable increase in their size and quality. In conclusion, the proposed assumptions and modifications enhance the capability of the Landauer model by increasing the accuracy of the prediction of λ_{eff} for sintered samples. The dependence of analytical λ_{eff} and d_{rel} has been changed from linear to exponential; thus, the agreement between analytical and experimental results is improved substantially.

4. Summary and remarks

The presented work can be summarised in the following remarks:

1) Experimental, theoretical and numerical investigation of thermal conductivity has been performed for porous NiAl samples manufactured by spark plasma sintering under different process conditions.
2) The real representation of the sample's microstructure has been obtained by X-ray computed tomography analysis, and then transferred to the finite element framework of heat conduction. The samples have been investigated numerically in the context of structural and thermal features, i.e., tortuosity, local heat fluxes or deviation of angles of flow.
3) Numerical results of λ_{eff} have been compared with data from three well-known analytical models and, furthermore, by experimental results determined via the laser flash method. A serious disagreement of the presented data led to consideration of the additional resistance within the solid medium, localised in particle necks.
4) A special algorithm has been developed to reveal the neck spots within porous structures and to add the complementary resistance phase. The proposed methodology has been verified by a simple benchmark test showing the required efficiency.

5) Finite element simulations with various contents of the resistance phase and different magnitudes of thermal conductivity have confirmed the model's ability to achieve a satisfactory correspondence between numerical and experimental data.
6) Landauer's model has been modified by taking into account the interfacial thermal resistance of necks, by employing the Yang model with a linear dependence of the local thermal resistance and sample densification. The new model allows the reproduction of the correct behaviour of thermal conductivity of sintered NiAl samples with changing porosity.

Declaration of Competing Interest

The authors declare that they have no known competing financial interests or personal relationships that could have appeared to influence the work reported in this paper.

CRediT authorship contribution statement

Szymon Nosewicz: Conceptualization, Methodology, Software, Supervision, Validation, Formal analysis, Investigation, Writing – original draft. **Grzegorz Jurczak:** Software, Validation, Formal analysis, Investigation, Writing – original draft. **Tomasz Wejrzanowski:** Methodology, Software, Writing – original draft. **Samih Haj Ibrahim:** Investigation, Formal analysis. **Agnieszka Grabias:** Investigation, Software, Writing – original draft. **Witold Węglewski:** Software, Writing – original draft. **Kamil Kaszyca:** Investigation, Writing – original draft. **Jerzy Rojek:** Resources, Formal analysis, Supervision. **Marcin Chmielewski:** Investigation, Resources, Methodology, Conceptualization, Writing – original draft.

Acknowledgments

The authors would like to acknowledge the financial support of the National Science Centre (DEC-2019/35/B/ST8/03158).

Supplementary materials

Supplementary material associated with this article can be found, in the online version, at doi:10.1016/j.ijheatmasstransfer.2022.123070.

References

[1] N. Curry, M. Leitner, K. Körner, High-Porosity Thermal Barrier Coatings from High-Power Plasma Spray Equipment—Processing, Performance and Economics, Coatings 10 (2020) 957.
[2] S. Rashidi, J.A. Esfahani, N. Karimi, Porous materials in building energy technologies - A review of the applications, modelling and experiments, Renew. Sust. Energ. Rev. 91 (2018) 229–247.
[3] P. He, Y. Wu, Constructing of highly porous thermoelectric structures with improved thermoelectric performance, Nano Res 14 (2021) 3608–3615.
[4] J. Fu, H.R. Thomas, C. Li, Tortuosity of porous media: Image analysis and physical simulation, Earth-Sci. Rev. 212 (2021) 103439.
[5] W. Woodside, Calculation of the thermal conductivity of porous media, Can. J. Phys. 36 (7) (1958) 815–823.
[6] H.S. Carslaw, J.C. Jaeger, Conduction of Heat in Solids, Second Edition, Oxford University Press, 1986.
[7] D. Shou, J. Fan, F. Ding, Hydraulic permeability of fibrous porous media, Int. J. Heat Mass Transf. 54 (2011) 4009–4018.
[8] K.M. Graczyk, M. Matyka, Predicting porosity, permeability, and tortuosity of porous media from images by deep learning, Sci Rep 10 (2020) 21488.
[9] J. Floury, J. Carson, T.Q. Pham, Modelling Thermal Conductivity in Heterogeneous Media with the Finite Element Method, Food Bioprocess Technol 1 (2008) 161–170.
[10] H. Xu, B. Chen, P. Tan, W. Cai, W. He, D. Farrusseng, M. Ni, Modeling of all porous solid oxide fuel cells, Appl. Energy 219 (2018) 105–113.
[11] M. Bahrami, M. Yovanovich, R. Culham, Effective thermal conductivity of rough spherical packed beds, Int. J. Heat Mass Transf. 49 (19–20) (2006) 3691–3701.
[12] H. Zhang, Y. Zhao, F. Wang, D. Li, A 3D discrete element-finite difference coupling model for predicting the effective thermal conductivity of metal powder beds, Int. J. Heat Mass Transf. 132 (2019) 1–10.
[13] Y. Zhang, Z. Han, S. Wu, A. Rhamdhani, C. Guo, G. Brooks, A predictive study on effective thermal conductivity of sintered nickel powder under different thermal processing conditions, Int. J. Heat Mass Transf. 185 (2022) 122380.
[14] A. Birnboim, T. Olorunyolemi, Y. Carmel, Calculating the thermal conductivity of heated powder compacts, J. Am. Ceram. Soc. 84 (6) (2001) 1315–1320.
[15] J.P.M. Florez, M.B.H. Mantelli, G.G.V. Nuernberg, Effective thermal conductivity of sintered porous media: model and experimental validation, Int. J. Heat Mass Transf. 66 (2013) 868–878.
[16] J. Polansky, N. Jeffers, J. Punch, A hybrid approach for predicting the effective thermal conductivity of sintered porous materials, Int. J. Therm. Sci. 148 (2020) 106135.
[17] O.M. Ibrahim, A.H. Al-Saiafi, S. Alotaibi, Thermal conductivity of porous sintered metal powder and the Langmuir shape factor, Heat Mass Transf 57 (8) (2021) 1289–1304.
[18] D.S. Smith, J.M. Dosal, S. Oummadi, D. Nouguier, D. Vitiello, A. Alzina, B. Nait-Ali, Neck formation and role of particle-particle contact area in the thermal conductivity of green and partially sintered alumina ceramics, J. Eur. Ceram. Soc. 42 (2022) 1618–1625.
[19] M. Ashby, F. Swinkels, A second report on sintering diagrams, Acta Metall 29 (2) (1981) 259–281.
[20] N. Sakatani, K. Ogawa, M. Arakawa, S. Tanaka, Thermal conductivity of lunar regolith simulant JSC-1A under vacuum, Icarus 309 (2018) 13–24.
[21] D. Marcos-Gómez, J. Ching-Lloyd, M.R. Elizalde, W.J. Clegg, J.M. Molina-Aldareguia, Predicting the thermal conductivity of composite materials with imperfect interfaces, Compos Sci Technol 70 (2010) 2276–2283.
[22] Y. Dong, Ch.-A. Wang, Numerical calculations of effective thermal conductivity of porous ceramics by image-based finite element method, Front, Mater. Sci. 6 (1) (2012) 79–86.
[23] K.-Q. Li, D.-Q. Li, Y. Liu, Meso-scale investigations on the effective thermal conductivity of multi-phase materials using the finite element method, Int. J. Heat Mass Transf. 151 (2020) 119383.
[24] W. Węglewski, P. Pitchai, M. Chmielewski, P.J. Guruprasad, M. Basista, Thermal conductivity of Cu-matrix composites reinforced with coated SiC particles: Numerical modeling and experimental verification, Int. J. Heat Mass Transf. 188 (2022) 122633.
[25] Y.T. Feng, K. Han, D.R.J. Owen, Discrete thermal element modelling of heat conduction in particle systems: Basic formulations, J. Comput. Phys. 227 (2008) 5072–5089.
[26] Y.T. Feng, K. Han, D.R.J. Owen, Discrete thermal element modelling of heat conduction in particle systems: Pipe-network model and transient analysis, Powder Technol 193 (2009) 248–256.
[27] M. Bahrami, M. Yovanovich, R. Culham, Effective thermal conductivity of rough spherical packed beds, Int. J. Heat Mass Transf. 49 (19–20) (2006) 3691–3701.
[28] H. Wu, N. Gui, X. Yang, J. Tu, S. Jiang, Numerical simulation of heat transfer in packed pebble beds: CFD-DEM coupled with particle thermal radiation, Int. J. Heat Mass Transf. 110 (2017) 393–405.
[29] C. Veyhl, I.V. Belova, G.E. Murch, T. Fiedler, Finite element analysis of the mechanical properties of cellular aluminium based on micro-computed tomography, Mater. Sci. Eng. 528 (2011) 4550–4555.
[30] T. Fiedlera, C. Veyhla, I.V. Belovaa, T. Bernthalerb, B. Heineb, G.E. Murcha, Mechanical properties and micro-deformation of sintered metallic hollow sphere structure, Comput. Mater. Sci. 74 (2013) 143–147.
[31] L. Han, S.H. Spangsdorf, N.V. Nong, L.T. Hung, Y.B. Zhang, H.N. Pham, Y.Z. Chen, A. Roch, L. Stepien, N. Pryds, Effects of spark plasma sintering conditions on the anisotropic thermoelectric properties of bismuth antimony telluride, RSC Advances 6 (2016) 59565–59573.
[32] J. Trapp, B. Kieback, Fundamental principles of spark plasma sintering of metals: part I – Joule heating controlled by the evolution of powder resistivity and local current densities, Powder Metallurgy 62 (5) (2019) 297–306.
[33] N.W. Solis, P. Peretyagin, A. Seleznev, R. Torrecillas, J.S. Moya, Black Zirconia–Graphene Nanocomposite Produced by Spark Plasma Sintering, AIP Conf. Proc. 1785 (2016) 040074.
[34] S. Min, J. Blumm, A. Lindeman, A new laser flash system for measurement of the thermophysical properties, Thermochimica Acta 455 (1–2) (2007) 46–49.
[35] A.M. Hofmeister, Measurements, Mechanisms, and Models of Heat Transport, Elsevier Inc, 2019.
[36] J.L.Feldman P.B.Allen, Thermal conductivity of disordered harmonic solids, Physical Review B 48 (17) (1993) 12581–12588.
[37] Y. Terada, K. Ohkubo, T. Mohri, T. Suzuki, Thermal Conductivity of Intermetallic Compounds with Metallic Bonding, Materials Transactions 43 (12) (2002) 3167–3176.
[38] S. Ashcraft-Anderson, The thermal conductivity of intermetallics, MSc Dissertation, Department of Materials Engineering, University of Cape Town, 1996.
[39] D.S. Smith, A. Alzina, J. Bourret, B. Nait-Ali, F. Pennec, N. Tessier-Doyen, K. Otsu, H. Matsubara, P. Elser, U.T. Gonzenbach, Thermal conductivity of porous materials, in: J. Mater. Res., 28, 2013, pp. 2260–2272.
[40] C.-W. Nan, R. Birringer, Determining the Kapitza resistance and the thermal conductivity of polycrystals: A simple model, Phys. Rev. B 57 (1998) 8264–8268.
[41] R. Askari, S. Taheri, S.H. Hejazi, Thermal conductivity of granular porous media: A pore scale modeling approach, AIP Advances 5 (2015) 097106.
[42] I. Savija, J.R. Culham, M.M. Yovanovich, Review of Thermal Conductance Models for Joints Incorporating Enhancement Materials, J Thermophys Heat Trans 17 (2003) 43–52.

[43] M.M. Fyrillas, C. Pozrikidis, Conductive heat transport across rough surfaces and interfaces between two conforming media, Int. J. Heat Mass Transf. 44 (2001) 1789–1801.
[44] M.A. Lambert, L.S. Fletcher, Thermal Contact Conductance of Non-Flat, Rough, Metallic Coated Metals, J. Heat Transfer 124 (2002) 405–412.
[45] H. Dong, B. Wen, R. Melnik, Relative importance of grain boundaries and size effects in thermal conductivity of nanocrystalline materials, Sci Rep 4 (2014) 7037.
[46] H.-S. Yang, G.-R. Bai, L.J. Thompson, J.A. Eastman, Interfacial thermal resistance in nanocrystalline yttria-stabilized zirconia, Acta Mater 50 (9) (2002) 2309–2317.
[47] J.W. Lawson, M.S. Daw, T.H. Squire, C.W. Bauschlicher, Computational Modeling of Grain Boundaries in ZrB2: Implications for Lattice Thermal Conductivity, J. Am. Ceram. Soc. 95 (2012) 3971–3978.
[48] F. Badry, K. Ahmed, A new model for the effective thermal conductivity of polycrystalline solids, AIP Advances 10 (2020) 105021.
[49] S. Nosewicz, J. Rojek, S. Mackiewicz, M. Chmielewski, K. Pietrzak, B. Romelczyk, The influence of hot pressing conditions on mechanical properties of nickel aluminide/alumina composite, J. Compos. Mater. 48 (2014) 3577–3589.
[50] P.G. Collishaw, J.R.G. Evans, An assessment of expressions for the apparent thermal conductivity of cellular materials, J. Mater. Sci. 29 (1994) 2261–2273.
[51] Z. Hashin, S. Shtrikman, A variational approach to the theory of the effective magnetic permeability of multiphase materials, J. Appl. Phys. 33 (1962) 3125–3131.
[52] I.-L. Ngo, S.V. Prabhakar Vattikuti, C. Byon, A modified Hashin-Shtrikman model for predicting the thermal conductivity of polymer composites reinforced with randomly distributed hybrid fillers, Int. J. Heat Mass Transf. 114 (2017) 727–734.
[53] R. Landauer, The electrical resistance of binary metallic mixtures, J. Appl. Phys. 23 (1952) 779–784.
[54] D.E. Angelescu, M.C. Cross, M.L. Roukes, Heat transport in mesoscopic systems, Superlattice. Microst. 23 (1998) 673–689.
[55] L.G.C. Rego, G. Kirczenow, Quantized Thermal Conductance of Dielectric Quantum Wires, Phys. Rev. Lett. 81 (1998) 232.
[56] Simpleware Software ScanIP/FE v.4.3, Simpleware Ltd, Exeter, UK, 2011.
[57] M. Basista, W. Węglewski, K. Bochenek, Z. Poniżnik, Z. Nowak, Micro-CT Finite Element Analysis of Thermal Residual Stresses and Fracture in Metal-Ceramic Composites, Adv. Eng. Mater. 19 (2017) 1–9.
[58] C. Pelissou, J. Baccou, Y. Monerie, F. Perales, Determination of the size of the representative volume element for random quasi-brittle composites, Int. J. Solids Struct. 46 (2009) 14–15.
[59] M. Chmielewski, S. Nosewicz, K. Pietrzak, J. Rojek, A. Strojny-Nędza, S. Mackiewicz, J. Dutkiewicz, Sintering behavior and mechanical properties of NiAl, Al_2O_3, and NiAl-Al_2O_3 composites, J. Mater. Eng. Perform. 23 (2014) 3875–3886.
[60] M. Smith, ABAQUS/Standard User's Manual, Version 6.9, Dassault Systemes Simulia Corp, United States, 2009.
[61] K. Yang, M. Li, N.N.A. Ling, F.L. May, P.R.J. Connolly, L. Esteban, M.B. Clennell, M. Mahmoud, A. El-Husseiny, A.R. Adebayo, M.M. Elsayed, M.L. Johns, Quantitative tortuosity measurements of carbonate rocks using pulsed field gradient NMR, Transp. Porous 130 (2019) 847–865.
[62] N.A. Zacharias, D.R. Nevers, C. Skelton, K. Knackstedt, D.E. Stephenson, D.R. Wheeler, Direct Measurements of Effective Ionic Transport in Porous Li-Ion Electrodes, J. Electrochem. Soc. 160 (2013) A306.
[63] S. Kolitcheff, E. Jolimaitre, A. Hugon, J. Verstraete, P. Carrette, M. Tayakout-Fayolle, Tortuosity of mesoporous alumina catalyst supports: Influence of the pore network organization, Microporous Mesoporous Mater 248 (2017) 91–98.
[64] T. Zielinski, Inverse identification and microscopic estimation of parameters for models of sound absorption in porous ceramics, in: Proceedings of International Conference on Noise and Vibration Engineering (ISMA2012)/International Conference on Uncertainty in Structural Dynamics (USD2012), 2012, pp. 95–108.
[65] O. Stenzel, O. Pecho, L. Holzer, M. Neumann, V. Schmidt, Predicting efective conductivities based on geometric microstructure characteristics, AIChE J 62 (2016) 1834–1843.
[66] R.I. Al-Raoush, I.T. Madhoun, Tort3d: A matlab code to compute geometric tortuosity from 3d images of unconsolidated porous media, Powder Technol 320 (2017) 99–107.
[67] O.O. Taiwo, D.P. Finegan, D.S. Eastwood, J.L. Fife, L.D. Brown, J.A. Darr, P.D. Lee, D.J. Brett, P.R. Shearing, Comparison of three-dimensional analysis and stereological techniques for quantifying lithium-ion battery electrode microstructures, J. Microsc. 263 (2016) 280–292.
[68] B. Tjaden, D.J. Brett, P.R. Shearing, Tortuosity in electrochemical devices: a review of calculation approaches, Int. Mater. Rev. 63 (2018) 47–67.
[69] R. Olives, S. Mauran, A highly conductive porous medium for solid–gas reactions: effect of the dispersed phase on the thermal tortuosity, Transp. Porous Media 43 (2001) 377–394.
[70] S. Cooper, D. Eastwood, J. Gelb, G. Damblanc, D. Brett, R. Bradley, P. Withers, P. Lee, A. Marquis, N. Brandon, P.R. Shearing, Image based modelling of microstructural heterogeneity in lifepo4 electrodes for li-ion batteries, J. Power Sources 247 (2014) 1033–1039.
[71] X. Song, X. Liu, J. Zhang, Neck formation and self-adjusting mechanism of neck growth of conducting powders in Spark Plasma Sintering, J. Am. Ceram. Soc. 89 (2) (2006) 494–500.
[72] H. Dai, D. Chen, Z. Zheng, Modelling the sintering neck growth process of metal fibers under the surface diffusion mechanism using the Lattice Boltzmann Method, Metals 9 (2019) 614.
[73] D. Demirskyi, D. Agrawala, A. Ragulya, Neck growth kinetics during microwave sintering of copper, Scr. Mater 62 (2010) 552–555.
[74] F. Ternero, L. Guerra Rosa, P. Urban, J.M. Montes, F.G. Cuevas, Influence of the total porosity on the properties of sintered, materials – A Review, Metals 11 (2021) 730.
[75] E. Torresani, D. Giuntini, C. Zhu, T. Harrington, K.S. Vecchio, A. Molinari, R.K. Bordia, E.A. Olevsky, Anisotropy of mass transfer during sintering of powder materials with pore – particle structure orientation, Metall. Mater. Trans. A 50A (2019) 1033–1049.
[76] M.B. Clennell, Tortuosity: a guide through the maze, Geol. Soc. Lond., Spec. Publ. 122 (1997) 299–344.
[77] P. Bobrowski, Z. Pędzich, M. Faryna, Three-dimensional microstructural characterization of porous cubic zirconia, Micron 78 (2015) 73–78.
[78] S. Nosewicz, J. Rojek, M. Chmielewski, K. Pietrzak, Discrete element modeling and experimental investigation of hot pressing of intermetallic NiAl powder, Adv Powder Technol 28 (2017) 1745–1759.